Measuring carrier diffusion in MAPbl₃ solar cells with photocurrent-detected transient grating spectroscopy *⊗*

Zhenyu Ouyang ⑩ ; Zijian Gan ⑩ ; Liang Yan ⑩ ; Wei You ⑩ ; Andrew M. Moran ■ ⑩



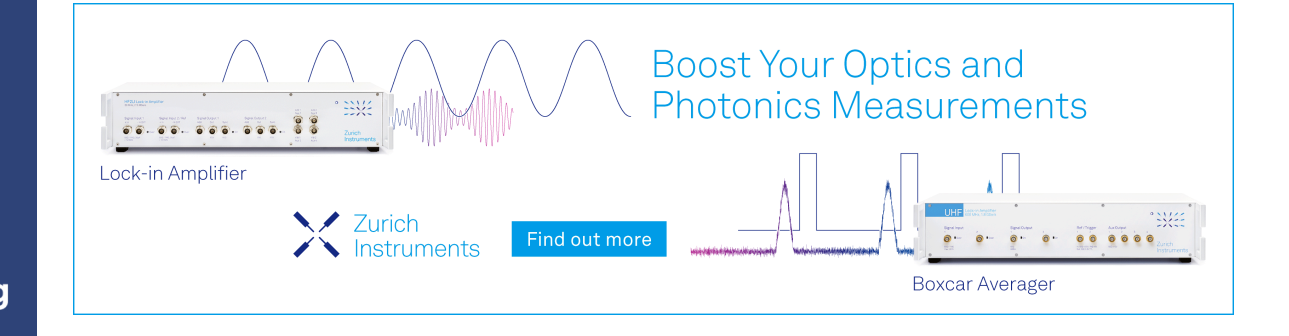
J. Chem. Phys. 159, 094201 (2023) https://doi.org/10.1063/5.0159301

6





02 June 2024 17:17:12





Measuring carrier diffusion in MAPbl₃ solar cells with photocurrent-detected transient grating spectroscopy

Cite as: J. Chem. Phys. 159, 094201 (2023); doi: 10.1063/5.0159301 Submitted: 22 May 2023 • Accepted: 15 August 2023 •





Published Online: 5 September 2023







Zhenyu Ouyang, 📵 Zijian Gan, 📵 Liang Yan, 📵 Wei You, 📵 and Andrew M. Moran 🛭 📵





AFFILIATIONS

Department of Chemistry, University of North Carolina at Chapel Hill, Chapel Hill, North Carolina 27599, USA

a) Author to whom correspondence should be addressed: ammoran@email.unc.edu

ABSTRACT

Conventional time-of-flight methods can be used to determine carrier mobilities for photovoltaic cells in which the transit time between electrodes is greater than the RC time constant of the device. To measure carrier drift on sub-ns timescales, we have recently developed a two-pulse time-of-flight technique capable of detecting drift velocities with 100-ps time resolution in perovskite materials. In this method, the rates of carrier transit across the active layer of a device are determined by varying the delay time between laser pulses and measuring the magnitude of the recombination-induced nonlinearity in the photocurrent. Here, we present a related experimental approach in which diffractive optic-based transient grating spectroscopy is combined with our two-pulse time-of-flight technique to simultaneously probe drift and diffusion in orthogonal directions within the active layer of a photovoltaic cell. Carrier density gratings are generated using two timecoincident pulse-pairs with passively stabilized phases. Relaxation of the grating amplitude associated with the first pulse-pair is detected by varying the delay and phase of the density grating corresponding to the second pulse-pair. The ability of the technique to reveal carrier diffusion is demonstrated with model calculations and experiments conducted using MAPbI₃ photovoltaic cells.

Published under an exclusive license by AIP Publishing. https://doi.org/10.1063/5.0159301

I. INTRODUCTION

Knowledge of carrier transport mechanisms facilitates the development of materials used for optoelectronic applications. 1-Because drift and diffusion are related physical processes, ^{18,19} experimental techniques targeting either class of transport mechanism may be employed for materials characterizations based on the convenience of implementation. For example, charge carrier mobilities can be measured within photovoltaic cells using a variety of methods. 4,11,20-23 In a conventional time-of-flight experiment, carrier drift is initiated when the active layer of a photovoltaic cell absorbs a laser pulse in the vicinity of a transparent electrode, whereas the carrier transit time to a second electrode is reflected by the delayed rise of the photocurrent.^{20–23} The mobility of the material is determined by establishing the dependence of the drift velocity on the potential applied to the device.^{1,2} Alternatively, the complexities of device fabrication can be avoided by examining the diffusion of photoexcited species in isolated materials. For example, carrier diffusivities are obtained by measuring the

photoluminescence efficiencies and excited-state lifetimes for materials interfaced with electron and/or hole quenching layers.²⁴ In addition, transient absorption microscopies yield direct images carrier diffusion in films and crystals. 2,9,10,12,17,26,27 While these conventional approaches provide valuable insights, the development of methods capable of simultaneously probing drift and diffusion is motivated by studies of heterogeneous materials and/or systems with coexisting photoexcited species (e.g., excitons, free charge carriers).

For studies of various perovskite systems, we have recently developed a time-of-flight technique, termed nonlinear photocurrent (NLPC) spectroscopy, in which carrier drift velocities are determined by applying two laser pulses to a photovoltaic cell with an experimentally controlled delay time. ^{28–33} In this approach, the nonlinearity in the response of the device originates in recombination processes involving carriers photoexcited by separate laser pulses^{31–33} rather than a nonlinear optical effect.^{34–41} The first laser pulse initiates drift of electrons and holes to their respective electrodes, whereas the second pulse "probes" the transient concentrations of carriers remaining in the active layer as a function of the delay time. Unlike a conventional time-of-flight method, 22,23 the time resolution of the NLPC technique is limited by the timescale of carrier recombination (~100 ps) rather than the RC time constant of the device $(0.1-1 \mu s)^{42-44}$ The versatility of the NLPC method has been leveraged in studies of perovskite photovoltaic cells with active layer thicknesses of 50-500 nm and carrier transit times of $2-50 \text{ ns.}^{\frac{1}{2}8-32}$

Recent applications of NLPC spectroscopy demonstrate that conducting time-of-flight experiments with two laser pulses offers several advantages in information content.^{28–33} For example, in studies of layered perovskite systems, the wavelengths of the two laser pulses can be tuned into resonance with quantum wells possessing different thicknesses to reveal the specific phases of the material occupied while the carriers drift to the electrodes. ^{28–30} Spectroscopic signatures of charge transfer observed in multidimensional NLPC experiments resemble those associated with two-dimensional Fourier transform spectra. 45-52 In addition, NLPC experiments can be conducted with both co-propagating and counter-propagating beam geometries to characterize the amount of drift velocity dispersion accumulated by a charge distribution as it traverses the full thickness of the active layer.³² Much like nonlinear optical effects are diminished when laser pulses propagate in dispersive media,53 the NLPC signal generation mechanism is sensitive to broadening of the charge density during transport because the response of the photocurrent depends nonlinearly on the carrier density. 31,32

In this work, we present an experimental method in which a diffractive optic-based transient grating (TG) technique^{54–57} is combined with NLPC spectroscopy to simultaneously probe diffusion and drift in orthogonal directions within the active layer of a photovoltaic cell. As illustrated in Fig. 1, carrier transport mechanisms are initiated when time-coincident laser pulses photoexcite periodic density gratings in the active layer of a device. The amplitude of the density grating diminishes with time due to carrier diffusion into the valleys between concentration maxima. Unlike conventional TG spectroscopy, the nonlinear response is induced when a second density grating is generated by a delayed pulse-pair in the TG-NLPC technique. Because the phases of the two density gratings are controlled with interferometric precision, signatures of diffusion are encoded in the efficiencies of recombination processes involving carriers photoexcited by separate pulse-pairs. Below, we first extend a numerical model developed for two-pulse NLPC spectroscopy to define the TG-NLPC signal generation mechanism and establish a method for interpreting the experimental data. 31,32 In addition to confirming the signal generation mechanisms with control experiments, the sensitivity of TG-NLPC spectroscopy to carrier diffusion is demonstrated with MAPbI₃ photovoltaic cells.

II. EXPERIMENTAL METHODS

A. Materials and device fabrication

Hydriodic acid (HI) (57 wt. % in water without stabilizer) and n-butylamine in ethanol (1:1 by volume) were combined at 0 °C in an ice water bath for 1 hour to produce CH3(CH2)3NH3I (BAI). The crude product was obtained by slowly evaporating the solvent under reduced pressure at 60 °C for 1 h. The white powder form of BAI was then recrystallized in ethanol and washed with diethyl ether three times before drying it in a vacuum oven at 60 °C overnight. The powder was stored in a glove box with a nitrogen environment. Hydriodic acid (57 wt. % in water without stabilizer) and methylamine solution (40 wt. % in H₂O) were combined to synthesize CH₃NH₃I (MAI).

Glass substrates patterned with indium-doped tin oxide (ITO) with sheet resistances of 20 Ω /square were purchased from South China Science and Technology Company, Limited. The substrates were cleaned with an ultrasonic bath using deionized water, acetone, and 2-proponal (15 min for each solvent in the sequence). Subsequently, the substrates were dried under a stream of nitrogen gas and treated with UV-Ozone for 15 min. Hole transport layers were prepared using either PTAA [poly(triaryl amine) from Sigma-Aldrich] in toluene (2 mg/ml) or PEDOT:PSS [poly(3,4ethylenedioxythiophene) polystyrene sulfonate CleviosTM P VP Al 4083 from Heraeus] aqueous dispersion in air. The solutions or dispersions were spin-coated onto the ITO substrates at 4000 rpm for 30 s and baked at either 100 °C for 10 min in a nitrogen-filled glove box (for PTAA) or 150 °C for 15 min in air (for PEDOT:PSS). After cooling down to room temperature, substrates coated with PEDOT:PSS were transferred into glove box filled with nitrogen gas. The perovskite precursor solution was then spin-coated onto substrates coated with PTAA or PEDOT:PSS under the nitrogen atmosphere.

Perovskite precursor solutions were prepared by dissolving PbI₂ and MAI in DMF:DMSO (9:1) to fabricate MAPbI₃ perovskite solar cells. The concentrations of Pb²⁺ required to produce 280- and

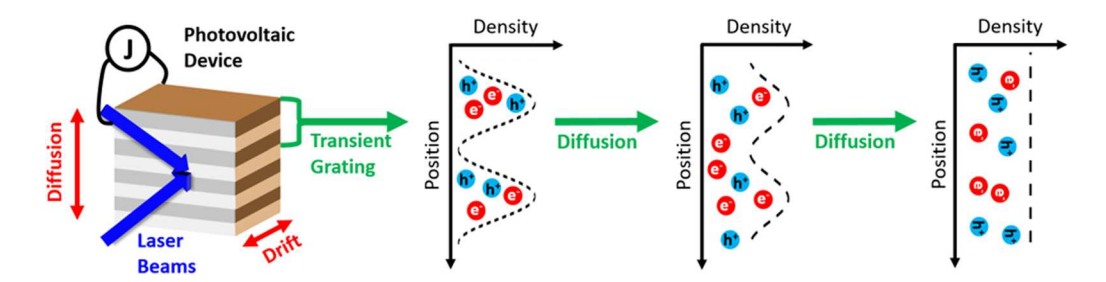


FIG. 1. Transient grating and nonlinear photocurrent techniques are combined to probe drift and diffusion in orthogonal spatial dimensions within photovoltaic cells. Noncollinear time-coincident laser pulses produce periodic carrier densities with passively stabilized phases in the active layer. The transient grating diminishes as carriers diffuse in a direction normal to drift between electrodes. Carrier diffusion processes are probed using a second density grating generated with a delayed pulse-pair (not shown).

480-nm thick films were 0.8 and 1.3M, respectively. The MAPbI₃ precursor solution was spin-coated onto a PTAA- or PEDOT:PSS-coated substrate (pre-wet by spin-coating pure dimethylformamide twice at 2000 rpm for 3 s for the PTAA-coated substrate) at 2000 rpm for 2 s and 4000 rpm for 20 s. The MAPbI₃ precursor solution (0.3 ml) was then drop-cast for 8 s in the second step of spin-coating. The sample was sequentially annealed at 65 °C for 10 min and 100 °C for 10 min. Finally, the electron transport layer and copper electrode were fabricated by thermally evaporating 40 nm of C₆₀, 4 nm of BCP (Bathocuproine), and 23 nm of copper at a base pressure of 3 \times 10⁻⁷ Torr with evaporation rates of 0.1–0.3, 0.1, and 0.1–0.2 Å/s, respectively. The active area of 0.13 cm² was controlled by a shadow mask.

The photovoltaic cells considered in this work are grouped according to the targeted active layer thicknesses of 280 and 480 nm. Like our previous work, 32 SEM measurements were used to confirm the active layer thicknesses with an estimated uncertainty of \sim 15% (see the supplementary material). Device characterization was carried out under AM 1.5 G irradiation with an intensity of 100 mW/cm² (Oriel 91160, 300 W). A Keithley 2400 digital source meter was used to obtain current density vs voltage (J-V) curves. The scan rates were 0.05 V/s.

B. Transient grating photocurrent spectrometer

The NLPC experiments reported in this work employ the PicoQuant diode laser system described in Ref. 32. The diode lasers are controlled with a single PicoQuant laser driver module (SEPIA II SLM 828) housed in a mainframe (PDL 828-L SEPIA II) and produce 400-nm, 40-ps laser pulses with energies of 100 pJ (LDH-P-C-405). Although the repetition rates of the lasers range from single shot to 80 MHz, all experiments are conducted at

5 kHz to ensure the Stanford Research Systems 570 current amplifier employed for signal detection reestablishes a baseline in the 200- μ s time interval between laser shots. The delay times between pulses produced by separate diode lasers are varied with a minimum step size of 24 ps using a PicoQuant oscillator module (SEPIA II SOM 828-D).

The diffractive optic-based interferometer depicted in Fig. 2 is used to conduct TG-NLPC experiments. Like a four-wave mixing experiment with interferometric signal detection, $^{54-57}$ the +/- 1 diffraction orders of the laser beams are imaged from the diffractive optic (Holoeye) to the sample position using a 4 F optical configuration. The custom diffractive optics (Holoeye) utilized in this work produce angles of either 4° or 8° between the +/- 1 diffraction orders at 400 nm. To minimize the spot sizes at the sample position, the diameters of the two laser beams are expanded by factors of 3 with telescopes incorporating lenses with -5 and +15 cm focal lengths before arriving at the interferometer. The beams are focused onto the diffractive optic using a 50-cm focal length spherical mirror with a silver coating. The vertically deflected +/-1 diffraction orders are then relayed to the sample with a 20-cm focal length, silvercoated spherical mirror placed 40 cm from the diffractive optic (i.e., at the 2 F position of the interferometer). The beams are directed to the sample position by tilting the 20-cm focal length mirror offaxis by $\sim 10^{\circ}$. Pulses with energies of 10–30 pJ pulses are focused to FWHM spot sizes of 60 μ m at the sample position, thereby producing fluences of 0.35–1.05 μ J/cm² for each of the four beams in the TG setup.

Passive phase stabilization of the pulse-pairs generated by the diffractive optic is achieved with this type of experimental setup. $^{54-57}$ For the first pulse-pair, the phase of the laser intensity profile at the sample position is controlled by placing a microscope coverslip at Brewster's angle in the path of the -1

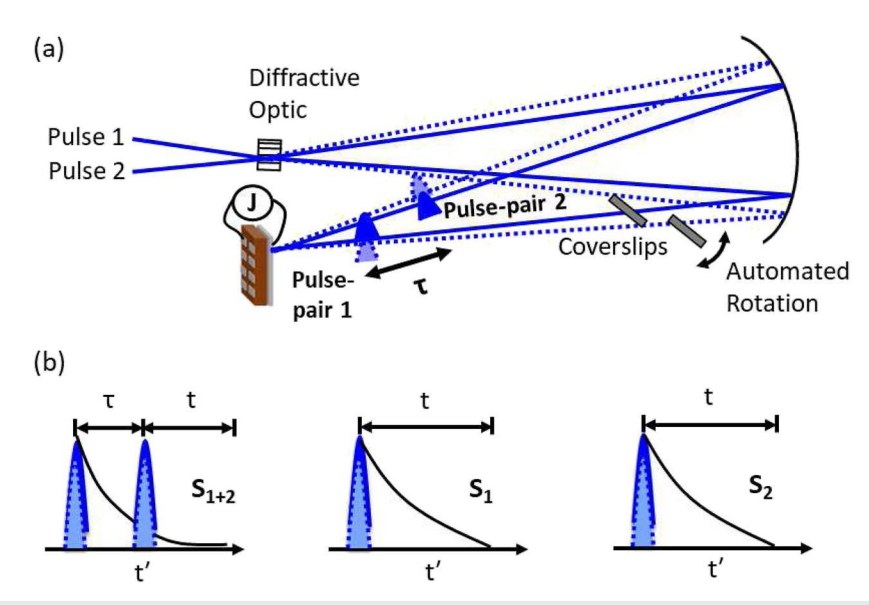


FIG. 2. (a) TG-NLPC measurements are conducted with a diffractive optic-based interferometer. The phase difference between the carrier density gratings produced by the first and second pulse-pairs is controlled with a microscope coverslip mounted on a motorized rotation stage. (b) The nonlinear response is defined by acquiring signals under four conditions: pulse-pairs 1 and 2 $[S_{1+2}(\tau)]$, pulse-pair 1 only (S_1) , pulse-pair 2 only (S_2) , and all pulses blocked (S_0) , not shown).

diffraction order (i.e., lower beam) and adjusting its orientation with a motorized rotation stage (Zaber X–RSW60A-E03). Rotating the glass coverslip by 0.23° induces a 360° phase shift of the carrier density grating within the active layer of a device, which has a negligible effect on the beam alignment. This approach for controlling the phase of the grating takes inspiration from interferometric signal detection methods employed in conventional diffractive optic-based TG experiments. 56,58–60 Notably, an identical coverslip with a fixed orientation is placed in the path of the beam associated with the +1 diffraction order (also at Brewster's angle) to ensure time-coincidence of the two pulses at the sample position.

As in earlier applications of our nonlinear action spectroscopies, 29-33 signals are acquired with a sequence of four conditions: pulse-pairs 1 and $2[S_{1+2}(\tau)]$, pulse-pair 1 only (S_1) , pulse-pair 2 only (S_2) , and all pulses blocked (S_0) . ^{28–31} The individual laser beams are turned on and off using LabVIEW software interfaced with the PicoQuant control system to cycle through the four conditions. Unlike NLPC experiments conducted with an amplified femtosecond laser system, 28-31,33 it is not necessary to chop the beams on a shot-to-shot basis due to the superior stabilities of the PicoQuant diode lasers.³² The signal, $S_{Action}(\tau) = S_{1+2}(\tau) - S_1 - S_2 + S_0$ represents the component of saturation induced by recombination processes involving carriers photoexcited by separate pulse-pairs. Therefore, only the signals detected with both pulse-pairs present, $S_{1+2}(\tau)$, depend on the experimentally controlled delay time. The signal-to-noise ratio is optimized by cycling through the four pulse sequences, 50 orientations of the microscope coverslip (with 0.024° steps), and 20-30 delay points a total of 5-12 times (depending on the signal quality) and averaging the data. Cycling through the full set of conditions 5 times results in a minimum data acquisition time of 4 h; however, the average data acquisition time for all datasets is equal to 7 h. Signals are saved for each cycle of the experimental conditions to confirm the devices do not degrade during the experiments (see the supplementary material). In addition, we do not observe phase instability on the timescale of several hours, which is consistent with our previous experience using similar diffractive optic-based interferometers in the same laboratory. 61,62 The overall time elapsed after the first pulse arrives at the device, t', is decomposed into an experimentally controlled delay time, τ , and current integration or "detection" time, t[see Fig. 2(b)].^{30,31}

The total amount of charge produced by a device is determined by time-integrating the amplified photocurrent. The photocurrent pulses are broadened to ~20 μ s with the 2- μ A/V sensitivity and gain mode (low noise) settings of the Stanford Research Systems 570 current amplifier employed in the present measurements. As discussed above, the bandwidth of the current amplifier ultimately limits the 5-kHz repetition rate of the laser system because it is necessary to reestablish a baseline between laser shots. In contrast, all photoexcited carriers are cleared from the active layers of the photovoltaic devices within ~1 μ s after light absorption. Signals are processed using a National Instruments data acquisition board (NI USB-6361) with a 1-MHz sampling rate (interval of 1 μ s between points). The total amount of charge collected from a device is computed by multiplying the time-integrated voltage output by the current-to-voltage amplification factor.

III. MODELING NONLINEAR PHOTOCURRENT SPECTROSCOPY WITH TRANSIENT DENSITY GRATINGS

In previous work, we presented a numerical model for simulating NLPC signals in both co-propagating and counter-propagating laser beam geometries. ^{31,32} Our approach, which takes inspiration from conventional TOF literature, ^{21,22,63,64} accounts for carrier drift, two-body recombination, and trap-induced velocity dispersion. For the present experiments involving transient density gratings, we introduce a more efficient numerical model in this section to facilitate calculations of NLPC signals with two spatial dimensions in the active layer of a device. Below, we first present an improved version of our model for two-pulse NLPC spectroscopy, then adapt the numerical approach to a transient grating beam geometry.

A. NLPC spectroscopy with two laser beams

Light enters the active layer of the device through a transparent electrode at x = 0. The carrier density initially possesses an exponential shape,

$$\rho(x,\omega_j,t') = \Theta(x)\Theta(d-x)\frac{f\alpha(\omega_j)}{\hbar\omega_j}\exp\left[-\alpha(\omega_j)x - t'/t_l\right], \quad (1)$$

where Θ is a Heaviside step function, d is the active layer thickness, ω_j is the frequency of laser pulse j (j = 1 or 2), $\alpha(\omega_j)$ is the absorbance coefficient, and t_l is the phenomenological lifetime of a free carrier. Whereas the initial distribution of charge is determined by the absorbance coefficient, the carrier densities subsequently decelerate and broaden while drifting to the electrodes because of trap-induced velocity dispersion. It is understood that accumulation of carriers at trap sites reduces the average drift velocity during transit across the active layer. For example, multiple-trapping models for carrier drift suggest the intrinsic, μ_0 , and effective, $\mu_{TOF}(t')$, mobilities are related by 22,63,64

$$\mu_{TOF}(t') = \mu_0 \frac{N_{free}(t')}{N_{free}(t') + N_{trap}(t')}, \tag{2}$$

where $N_{free}(t')$ and $N_{trap}(t')$ are time-dependent populations of free and trapped carriers, respectively. ^{22,63,64} To capture dispersive effects, we assume the drift velocity possesses an exponential decay profile, ³¹

$$v_{drift}(t', t_{trap}) = v_0 \exp(-t'/t_{trap}),$$
 (3)

where t_{trap} is written as a variable to account for a heterogeneous distribution of trapping times. The displacement in the carrier density at time, t', is given by

$$\Delta x(t', t_{trap}) = -\int_0^{t'} v_{drift}(T) dT$$
$$= v_0 t_{trap} \left[1 - \exp\left(-t'/t_{trap}\right) \right]. \tag{4}$$

The hole and electron densities photoexcited by the first $(\tilde{p}_1$ and $\tilde{n}_1)$ and second $(\tilde{p}_2$ and $\tilde{n}_2)$ laser pulses are written as

$$\tilde{p}_{1}(x,\omega_{1},t') = \frac{1}{\xi\sqrt{2\pi}} \int_{0}^{\infty} \exp\left[-\frac{\left(t_{trap} - \bar{t}_{trap}\right)^{2}}{2\xi^{2}}\right] \times \rho(x - \Delta x(t',t_{trap}),\omega_{1},t')dt_{trap},$$
 (5)

$$\tilde{n}_{1}(x,\omega_{1},t') = \frac{1}{\xi\sqrt{2\pi}} \int_{0}^{\infty} \exp\left[-\frac{\left(t_{trap} - \overline{t}_{trap}\right)^{2}}{2\xi^{2}}\right] \times \rho(x + \Delta x(t',t_{trap}),\omega_{1},t')dt_{trap}, \tag{6}$$

$$\tilde{p}_{2}(x,\omega_{2},t') = \frac{\Theta(t'-\tau)}{\xi\sqrt{2\pi}} \int_{0}^{\infty} \exp\left[-\frac{(t_{trap}-\bar{t}_{trap})^{2}}{2\xi^{2}}\right] \times \rho(x-\Delta x(t'-\tau,t_{trap}),\omega_{2},t')dt_{trap},$$
(7)

and

$$\tilde{n}_{2}(x,\omega_{2},t') = \frac{\Theta(t'-\tau)}{\xi\sqrt{2\pi}} \int_{0}^{\infty} \exp\left[-\frac{\left(t_{trap} - \overline{t}_{trap}\right)^{2}}{2\xi^{2}}\right] \times \rho(x + \Delta x(t'-\tau,t_{trap}),\omega_{2},t')dt_{trap},$$
(8)

where \bar{t}_{trap} is the mean trapping time and ξ is a phenomenological width set equal to $\bar{t}_{trap}/2$ in this work. Convolution of ρ with a distribution of trapping times eliminates nonphysical flat edges on the trailing sides of the carrier densities. Although dispersive effects were incorporated differently in our earlier model, the calculations discussed below show that the present approach yields densities with similar shapes. We have neglected two-body recombination dynamics associated with carriers photoexcited by individual laser pulses in Eqs. (5)–(8) to reduce computational expense. This approximation has minor effects on the shapes of the carrier densities because roughly 5% of carriers relax by two-body recombination under our experimental conditions. Moreover, the signals are time-integrated during the detection process, which makes the measurements relatively insensitive to the precise shapes of the carrier densities.

To minimize the computational cost associated with recombination-induced reshaping of the density profiles, 31,32 two-body recombination processes involving carriers photoexcited by separate laser pulses are incorporated using

$$p_{1}(x,\omega_{1},t') = \tilde{p}_{1}(x,\omega_{1},t') - \tilde{p}_{1}(x,\omega_{1},t') \cdot \beta \cdot \Delta t'$$

$$\cdot \int_{\tau}^{t'} \frac{\int_{0}^{d} \tilde{p}_{1}(x,\omega_{1},T) \tilde{n}_{2}(x,\omega_{2}T) dx}{\int_{0}^{d} \tilde{p}_{1}(x,\omega_{1},T) dx} dT, \qquad (9)$$

$$n_{1}(x,\omega_{1},t') = \tilde{n}_{1}(x,\omega_{1},t') - \tilde{n}_{1}(x,\omega_{1},t') \cdot \beta \cdot \Delta t'$$

$$\cdot \int_{0}^{t'} \frac{\int_{0}^{d} \tilde{n}_{1}(x,\omega_{1},T) \tilde{p}_{2}(x,\omega_{2},T) dx}{\int_{0}^{d} \tilde{n}_{1}(x,\omega_{1},T) dx} dT, \qquad (10)$$

$$p_{2}(x,\omega_{2},t') = \tilde{p}_{2}(x,\omega_{2},t') - \tilde{p}_{2}(x,\omega_{2},t') \cdot \beta \cdot \Delta t'$$

$$\cdot \int_{\tau}^{t'} \frac{\int_{0}^{d} \tilde{n}_{1}(x,\omega_{1},T) \tilde{p}_{2}(x,\omega_{2},T) dx}{\int_{0}^{d} \tilde{p}_{2}(x,\omega_{2},T) dx} dT, \qquad (11)$$

and

$$n_{2}(x, \omega_{2}, t') = \tilde{n}_{2}(x, \omega_{2}, t') - \tilde{n}_{2}(x, \omega_{2}, t') \cdot \beta \cdot \Delta t'$$

$$\cdot \int_{\tau}^{t'} \frac{\int_{0}^{d} \tilde{p}_{1}(x, \omega_{1}, T) \tilde{n}_{2}(x, \omega_{2}, T) dx}{\int_{0}^{d} \tilde{n}_{2}(x, \omega_{2}, T) dx} dT.$$
(12)

The two-body recombination coefficient and numerical time interval are denoted as β and $\Delta t'$, respectively. Compared to our previous numerical model, 31,32 the efficiency of the present approach has been improved by spatial averaging of the targeted recombination rates, $\beta \tilde{p}_1 \tilde{n}_2$ and $\beta \tilde{n}_1 \tilde{p}_2$, in Eqs. (9)–(12). Transient absorption experiments conducted on similar solution-processed perovskite films revealed dominant quadratic dependence of the recombination rates on the carrier densities.2 Trap-assisted band-to-band recombination is typically described as scaling linearly in the carrier density because one of the charges is immobile;6 however, this recombination process involves two photoexcited species and may represent a significant contribution to β for NLPC experiments. Quadratic scaling of recombination rates with the carrier density is also consistent with radiative and trap-assisted Auger recombination.6

Nonlinear photocurrent signals are obtained by computing the response of the device under three conditions.^{29–32} The amounts of charge collected from the photovoltaic cell with the two individual pulses are given by

$$q_{1}(\omega_{1}) = \frac{eA}{\Delta t'} \left\{ \int_{0}^{\infty} dt' \int_{d-\Delta x(t',\bar{t}_{\nu})}^{d} \tilde{n}_{1}(x,\omega_{1},t') dx + \int_{0}^{\infty} dt' \int_{0}^{\Delta x(t',\bar{t}_{\nu})} \tilde{p}_{1}(x,\omega_{1},t') dx \right\}$$
(13)

and

$$q_{2}(\omega_{2}) = \frac{eA}{\Delta t'} \left\{ \int_{0}^{\infty} dt' \int_{d-\Delta x \left(t'-\tau,\bar{t}_{\nu}\right)}^{d} \tilde{n}_{2}(x,\omega_{2},t') dx + \int_{0}^{\infty} dt' \int_{0}^{\Delta x \left(t'-\tau,\bar{t}_{\nu}\right)} \tilde{p}_{2}(x,\omega_{2},t') dx \right\},$$
(14)

where A is the area of the laser spot on the device. The amount of charge collected with both pulses incident on the photovoltaic cell is written as

$$q_{1+2}(\omega_1, \tau, \omega_2) = \frac{eA}{\Delta t'} \left\{ \int_0^\infty dt \int_{d-\Delta x(t', \bar{t}_v)}^d n_1(x, \omega_1, \tau + t) dx + \int_0^\infty dt \int_{d-\Delta x(t'-\tau, \bar{t}_v)}^d n_2(x, \omega_1, \tau + t) dx + \int_0^\infty dt \int_0^{\Delta x(t', \bar{t}_v)} p_1(x, \omega_2, \tau + t) dx + \int_0^\infty dt \int_0^{\Delta x(t'-\tau, \bar{t}_v)} p_2(x, \omega_2, \tau + t) dx \right\}.$$
(15)

Finally, the two-pulse NLPC signal is given by the linear combination of terms,

$$\Delta q_{NLPC}(\omega_1, \tau, \omega_2) = q_{1+2}(\omega_1, \tau, \omega_2) - q_1(\omega_1) - q_2(\omega_2). \tag{16}$$

Propagation of the hole and electron densities is illustrated in Figs. 3(a) and 3(b) using the model parameters in Table I. The carrier density decelerates [see Eqs. (3) and (4)] and broadens during transit due to numerous cycles of capture and release at trap sites [see Eqs. (5)–(8)]. 22,63,64 The concentrations of carriers photoexcited by the first laser pulse decrease as the species drift to the electrodes during the experimentally controlled delay time, τ , which reduces the rates of the recombination processes responsible for signal generation [i.e., $\beta \bar{p}_1 \bar{n}_2$ and $\beta \bar{n}_1 \bar{p}_2$ in Eqs. (9)–(12)]. Therefore, time-of-flight information is reflected by the NLPC decay profile [see Fig. 3(c)]. $^{29-32}$ The effects of trapping and drift velocity dispersion on photovoltaic device efficiencies have been examined in earlier NLPC experiments conducted on a variety of perovskite systems. 31 Overall, the calculations in Fig. 3 demonstrate that key aspects of our earlier model are still captured under the present approximations. 31,32

B. NLPC spectroscopy with a transient grating beam geometry

In this section, we generalize the model presented in Sec. III A to two spatial dimensions for measurements involving transient density gratings. As shown in Fig. 4, the light intensity profile is modulated in the *y*-dimension (i.e., parallel to the active layer surface) due to interference between noncollinear laser pulses, whereas drift occurs along the *x*-axis between electrodes. The grating patterns gradually diminish due to diffusion, recombination, and injection of carriers into the electrodes. The TG-NLPC technique is sensitive to

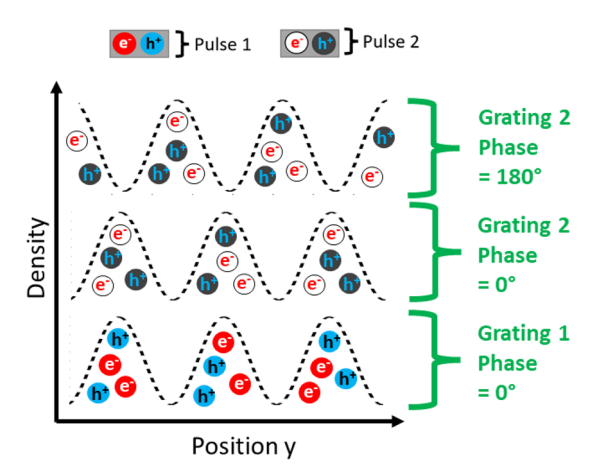


FIG. 4. Transient carrier density gratings are generated and probed using two phase-stabilized pulse-pairs. (a) The first pulse-pair initiates carrier diffusion in the y-dimension, whereas drift occurs along the x-axis within the active layer. Although relative phases of 0° and 180° are shown here, the phase difference between gratings is varied with ~ten points per cycle in the experimental measurements.

diffusion because the efficiencies of recombination processes involving carriers generated by separate pulse-pairs depend on the phase difference between the gratings. For example, the greatest and smallest amounts of device saturation are found when the two gratings have phase differences of 0° and 180° , respectively. Therefore, the amplitude of the transient grating generated by the first pulse-pair can be probed by varying the relative phase and delay time for the second pulse-pair.

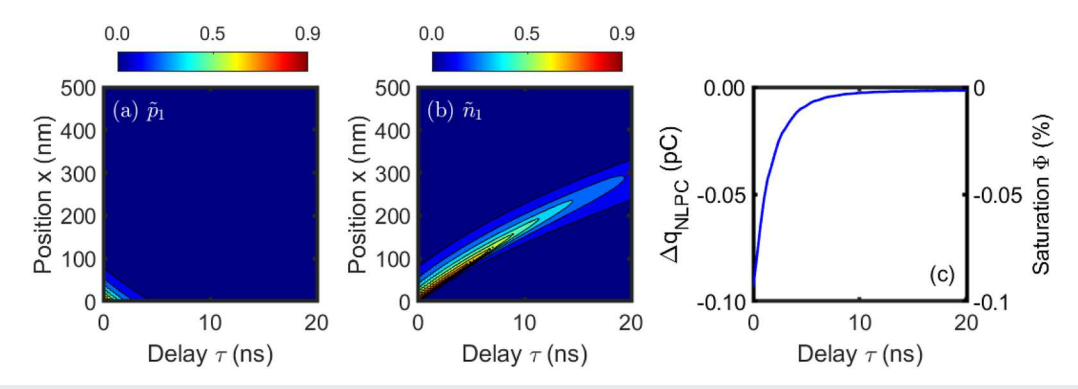


FIG. 3. Photoexcited (a) hole \tilde{p}_1 and (b) electron \tilde{n}_1 densities are calculated using Eqs. (5) and (6). The color bars are scaled by factors of 10^{17} cm⁻³. (c) A two-pulse NLPC decay profile is computed using Eq. (16) and the parameters in Table I.

TABLE I. Model parameters.

$\frac{f\alpha(\omega_j)}{\hbar\omega_j}$	α^{-1a}	β	κ_{ref}^{a}	t_l	ν_0	\overline{t}_{trap}	ξ	A	w	L_{j}
$1 \times 10^{17} \text{ cm}^{-3}$	34 nm	$10^{-9} \text{ cm}^3/\text{s}$	2.67	50 ns	20 m/s	20 ns	$t_{trap}/2$	$2827 \mu \text{m}^2$	25 μm	1.07 μm

^aThe absorbance coefficient and refractive index are obtained from Ref. 69.

We next present an approach for computing signals in which periodic carrier densities are photoexcited by separate pulse-pairs. The *y*-dimension of the carrier density is given by the product of the Gaussian laser profile and dynamic grating pattern,

$$G(y, t', \phi_j) = \chi^{-1}(t') \exp\left(-\frac{y^2}{2w^2}\right) \left\{1 + \exp\left(-\frac{t'}{t_{diff}}\right) \times \left[\cos^2\left(\frac{\pi y}{L} + \frac{\phi_j}{2}\right) - 1\right]\right\}, \tag{17}$$

where

$$\chi(t') = \int_{-\infty}^{\infty} \exp\left(-\frac{y^2}{2w^2}\right) \left\{ 1 + \exp\left(-\frac{t'}{t_{diff}}\right) \times \left[\cos^2\left(\frac{\pi y}{L} + \frac{\phi_j}{2}\right) - 1\right] \right\} dy.$$
 (18)

In Eq. (17), w is the laser spot size on the device, t_{diff} is the relaxation timescale for the grating, and ϕ_j is the phase of the grating generated by pulse-pair j. The period of the density grating, L, is computed using the angle between laser beams, θ , and the refractive index for the material, κ_{ref} ,

$$L = \frac{\lambda}{2\kappa_{ref} \sin\left(\theta/2\right)}. (19)$$

Gratings generated by both pulse-pairs possess the same period, L, because of their identical wavelengths, λ , and crossing angles, θ .

The grating relaxation time, $t_{\it diff}$, is determined by solving the diffusion equation,

$$\frac{\partial \Lambda(y,t)}{\partial t} = D \frac{\partial^2 \Lambda(y,t)}{\partial y^2},$$
 (20)

with the initial condition given by

$$\Lambda(y,0) = \Lambda_0 \exp\left(-\frac{y^2}{2w^2}\right) \cos^2\left(\frac{\pi y}{L}\right),\tag{21}$$

where Λ_0 is the peak carrier density, D is the diffusion coefficient, w is the laser spot size, and L is the period of the grating. The total density, $\Lambda(y,t)$, represents a sum of time-evolving Gaussian, $u_G(y,t)$, and periodic, $u_p(y,t)$, components that reflect the spatial profiles of the laser beams and grating amplitudes, respectively. To obtain the relaxation timescale for the transient grating, the carrier density is first Fourier transformed into the conjugate domain, k, with

$$\tilde{\Lambda}(k,t) = \int_{-\infty}^{\infty} \Lambda(y,t) \exp(-iky) dy.$$
 (22)

The Gaussian component of the density grating is then given by the inverse Fourier transform of the product of $\tilde{\Lambda}(k,t)$ and a Gaussian apodization function, a(k),

$$u_G(y,t) = \int_{-\infty}^{\infty} a(k) \cdot \bar{\Lambda}(k,t) \exp(iky) dk.$$
 (23)

To separate the Gaussian and periodic components of the density, the apodization function, a(k), is parameterized with a standard deviation of 1.29 rad/ μ m and w is set equal to 25.4 μ m. The periodic component of the carrier density is written as

$$u_p(y,t) = \Lambda(y,t) - u_G(y,t). \tag{24}$$

The value of t_{diff} is found by least-squares fitting the periodic component of the density, $u_p(0,t)$, to a single exponential function (see the supplementary material). As shown in Fig. 5, the relationship between D and t_{diff} is established numerically with this method using parameters corresponding to the experimental conditions (e.g., grating period and laser spot size). Because t_{diff} can be obtained by fitting experimental data, the calculation in Fig. 5 will be employed to determine empirical diffusion coefficients in our analysis of the TG-NLPC data presented below.

With this approach for computing the diffusion time, the carrier densities photoexcited with a transient grating beam geometry can be written as

$$P_{1}(x,\omega_{1},t',\phi_{1},\phi_{2}) = \tilde{p}_{1}(x,\omega_{1},t') - \tilde{p}_{1}(x,\omega_{1},t') \frac{\chi^{2}(t')\beta \cdot \Delta t'}{w\sqrt{\pi}} \cdot \int_{\tau}^{t'} \frac{\int_{-\infty}^{\infty} G(y,t',\phi_{1})G(y,t',\phi_{2})dy \int_{0}^{d} \tilde{p}_{1}(x,\omega_{1},T)\tilde{n}_{2}(x,\omega_{2},T)dx}{\int_{-\infty}^{\infty} G(y,t',\phi_{1})dy \int_{0}^{d} \tilde{p}_{1}(x,\omega_{1},T)dx} dT, \qquad (25)$$

$$N_{1}(x,\omega_{1},t',\phi_{2},\phi_{2}) = \tilde{n}_{1}(x,\omega_{1},t') - \tilde{n}_{1}(x,\omega_{1},t') \frac{\chi^{2}(t')\beta \cdot \Delta t'}{w\sqrt{\pi}} \cdot \int_{0}^{t'} \frac{\int_{-\infty}^{\infty} G(y,t',\phi_{1})G(y,t',\phi_{2})dy \int_{0}^{d} \tilde{n}_{1}(x,\omega_{1},T)\tilde{p}_{2}(x,\omega_{2},T)dx}{\int_{-\infty}^{\infty} G(y,t',\phi_{1})dy \int_{0}^{d} \tilde{n}_{1}(x,\omega_{1},T)dx} dT,$$
 (26)

$$P_{2}(x,\omega_{2},t',\phi_{1},\phi_{2}) = \tilde{p}_{2}(x,\omega_{2},t') - \tilde{p}_{2}(x,\omega_{2},y,t') \frac{\chi^{2}(t')\beta \cdot \Delta t'}{w\sqrt{\pi}} \cdot \int_{-\infty}^{t'} \frac{\int_{-\infty}^{\infty} G(y,t',\phi_{1})G(y,t',\phi_{2})dy \int_{0}^{d} \tilde{n}_{1}(x,\omega_{1},T)\tilde{p}_{2}(x,\omega_{2},T)dx}{\int_{-\infty}^{\infty} G(y,t',\phi_{2})dy \int_{0}^{d} \tilde{p}_{2}(x,\omega_{2},T)dx} dT, \quad (27)$$

and

$$N_{2}(x,\omega_{2},t',\phi_{1},\phi_{2}) = \tilde{n}_{2}(x,y,\omega_{2},t') - \tilde{n}_{2}(x,y,\omega_{2},t') \frac{\chi^{2}(t')\beta \cdot \Delta t'}{w\sqrt{\pi}} \int_{\tau}^{t'} \frac{\int_{-\infty}^{\infty} G(y,t',\phi_{1})G(y,t',\phi_{2})dy \int_{0}^{d} \tilde{p}_{1}(x,\omega_{1},T)\tilde{n}_{2}(x,\omega_{2},T)dx}{\int_{-\infty}^{\infty} G(y,t',\phi_{2})dy \int_{0}^{d} \tilde{n}_{2}(x,\omega_{2},T)dx} dT.$$
 (28)

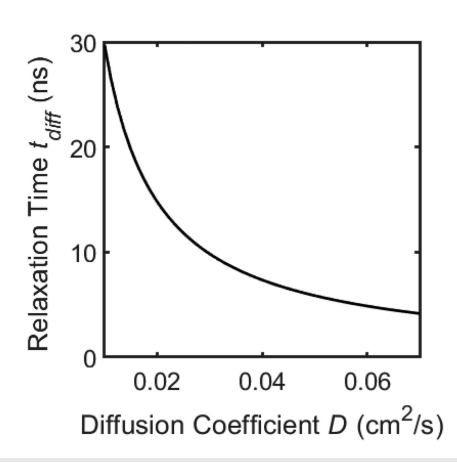


FIG. 5. Relaxation timescales for the transient density gratings, t_{diff} , are computed using Eqs. (17)–(24) for a range of diffusion coefficients, D, to establish a general relation between the two quantities. The grating period of L = 1.07 μ m corresponds to 400 nm laser beams, a crossing angle of $\theta = 8^{\circ}$, and a refractive index of 2.67.

In this notation, the carrier densities associated with the transient grating configuration are written in upper case to distinguish them from the conventional two-pulse NLPC technique [see Eqs. (9)–(12)]. Importantly, Eqs. (25)–(28) reduce to Eqs. (9)–(12) when the grating period is much greater than the laser spot size, $L\gg w$. Although we have written the full two-dimensional densities in the denominators of Eqs. (25)–(28), the individual grating functions, $G(y,t',\phi_j)$, are normalized according to Eqs. (17) and (18). Therefore, the targeted interference effect is produced by the integral over the product of grating functions in the numerators of Eqs. (25)–(28).

The total amounts of charge generated by the photovoltaic cell in response to the individual pulse-pairs are given by

$$Q_{1}(\omega_{1}) = \frac{e \cdot A}{\Delta t'} \left\{ \int_{0}^{\infty} dt' \int_{-\infty}^{\infty} G(y, t', \phi_{1}) dy \right.$$

$$\times \int_{d-\Delta x(t', \bar{t}_{y})}^{d} \tilde{n}_{1}(x, \omega_{1}, t', \phi_{1}) dx$$

$$+ \int_{0}^{\infty} dt' \int_{-\infty}^{\infty} G(y, t', \phi_{1}) dy$$

$$\times \int_{0}^{\Delta x(t', \bar{t}_{y})} \tilde{p}_{1}(x, \omega_{1}, t', \phi_{1}) dx \right\}$$

$$(29)$$

and

$$Q_{2}(\omega_{2}) = \frac{e \cdot A}{\Delta t'} \left\{ \int_{0}^{\infty} dt' \int_{-\infty}^{\infty} G(y, t', \phi_{2}) dy \right.$$

$$\times \int_{d-\Delta x(t'-\tau, \bar{t}_{v})}^{d} \tilde{n}_{2}(x, \omega_{2}, t') dx$$

$$+ \int_{0}^{\infty} dt' \int_{-\infty}^{\infty} G(y, t', \phi_{2}) dy$$

$$\times \int_{0}^{\Delta x(t'-\tau, \bar{t}_{v})} \tilde{p}_{2}(x, \omega_{2}, t') dx \right\}. \tag{30}$$

Notably, the two-beam and transient density grating approaches yield the same amounts of charge, $Q_1(\omega_2) = q_1(\omega_1)$ and $Q_2(\omega_2)$

= $q_2(\omega_1)$, because the grating functions are normalized and recombination processes involving carriers photoexcited by the individual pulses are neglected by approximation [see Eqs. (9)–(12)]. The amount of charge produced with both pulse-pairs incident on the photovoltaic cell is written as

$$Q_{1+2}(\omega_{1}, \tau, \omega_{2}, \phi_{1}, \phi_{2})$$

$$= \frac{e \cdot A}{\Delta t'} \left\{ \int_{0}^{\infty} dt \int_{d-\Delta x \left(t', \bar{t}_{\nu}\right)}^{d} N_{1}(x, \omega_{1}, \tau + t, \phi_{1}, \phi_{2}) dx + \int_{0}^{\infty} dt \int_{d-\Delta x \left(t'-\tau, \bar{t}_{\nu}\right)}^{d} N_{2}(x, \omega_{2}, \tau + t, \phi_{1}, \phi_{2}) dx + \int_{0}^{\infty} dt \int_{0}^{\Delta x \left(t', \bar{t}_{\nu}\right)} P_{1}(x, y, \omega_{1}, \tau + t, \phi_{1}, \phi_{2}) dx + \int_{0}^{\infty} dt \int_{0}^{\Delta x \left(t'-\tau, \bar{t}_{\nu}\right)} P_{2}(x, y, \omega_{2}, \tau + t, \phi_{1}, \phi_{2}) dx \right\}.$$
(31)

The nonlinear response in the amount of charge collected from the device is given by a linear combination of terms,

$$\Delta Q_{TG-NLPC}(\omega_1, \tau, \omega_2, \phi_1, \phi_2) = Q_{1+2}(\omega_1, \tau, \omega_2, \phi_1, \phi_2) - Q_1(\omega_1) - Q_2(\omega_2),$$
(32)

where we have distinguished the conventional two-pulse (NLPC) and transient density grating (TG-NLPC) approaches by writing the charges, Q, in upper case.

Drift and diffusion processes are simulated for a transient density grating with a period of 1.07 μ m in Fig. 6. The two-dimensional shapes of the densities are generated by multiplying the functions of x, \tilde{p}_1 and \tilde{n}_1 , with the periodic function of y, G(y,t',0). Like the calculations presented in Fig. 3, holes and electrons drift to their respective electrodes along the x-axis; however, the amplitude of the grating additionally relaxes in the y-dimension due to carrier diffusion on the timescale, t_{diff} . For example, a density grating with a period of 1.07 μ m diminishes with a time constant of $t_{diff} = 9.8$ ns when the diffusion coefficient is set equal to D = 0.03 cm²/s (see Fig. 5). Because drift must not outcompete diffusion in a successful TG-NLPC measurement, the total potential applied across the active layer should generally satisfy the relation

$$V < \frac{d}{\alpha \cdot \mu_{avg} \cdot t_{diff}},\tag{33}$$

where α is the absorbance coefficient, μ_{avg} is the average carrier mobility, and d is the active layer thickness. For example, according to Eq. (33), the total potential should not be greater than 0.68 V for a TG-NLPC experiment conducted using a device with the parameters $\alpha^{-1}=34$ nm, ⁶⁹ $t_{diff}=10$ ns, $\mu_{avg}=0.025$ cm²/V/s, ^{30,32} and d=500 nm. In principle, an external potential may be adjusted to improve the sensitivity of TG-NLPC measurements to carrier diffusion depending on the material's mobility and the active layer thickness.

Signals are computed as functions of both the delay time and phase difference between gratings photoexcited by separate pulsepairs in Fig. 7. Calculations are conducted with diffusion coefficients ranging from $D = 0.01-0.06 \text{ cm}^2/\text{s}$ to illustrate the sensitivity of the

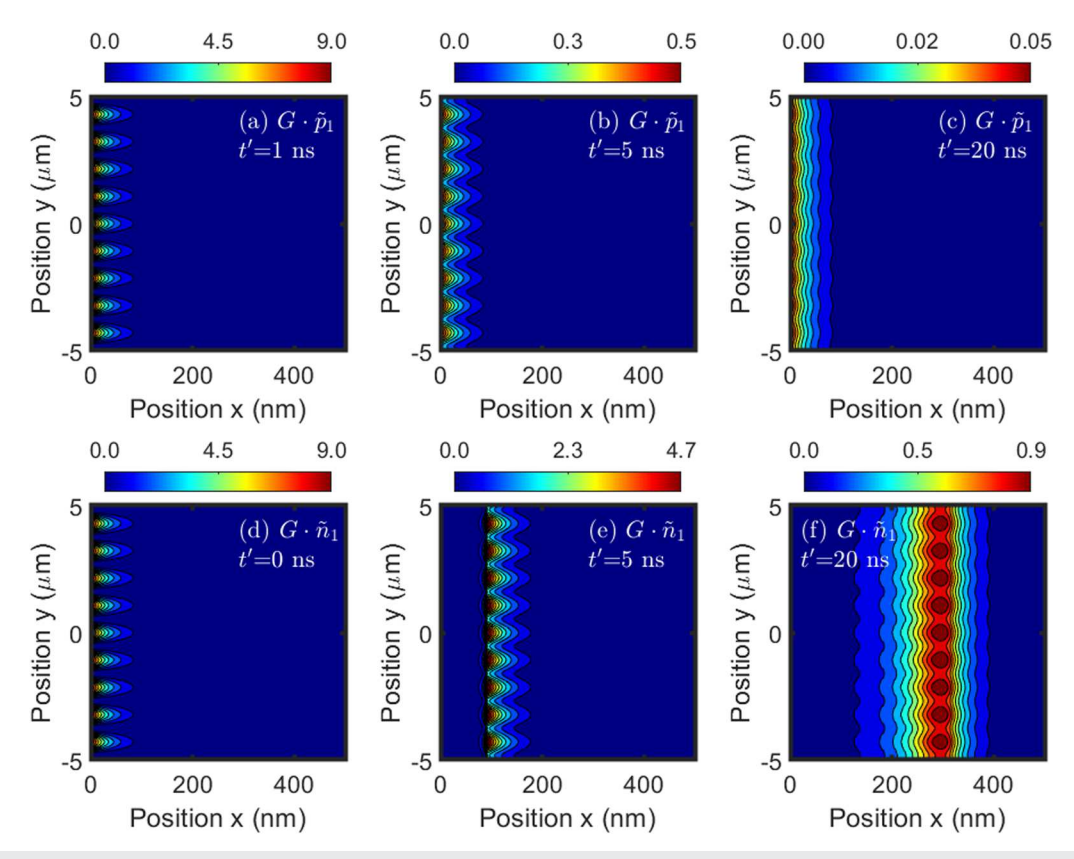


FIG. 6. Carrier drift and diffusion mechanisms are simulated for transient density gratings with 1.07- μ m periods using Eqs. (5), (6) and (17). Hole (top row) and electron (bottom row) densities are represented as $G(y, t', 0)\bar{p}_1(x, \omega_1, t')$ and $G(y, t', 0)\bar{n}_1(x, \omega_1, t')$ at the times, t', given in the respective figure panels. The carrier densities undergo drift and diffusion in the dimensions x and y, respectively. The grating relaxation time assumed in these calculations, $t_{diff} = 9.8$ ns, corresponds to a diffusion coefficient of D = 0.03 cm²/s, whereas the other parameters are given in Table I. The color bars are scaled by factors of 10^{14} cm⁻³.

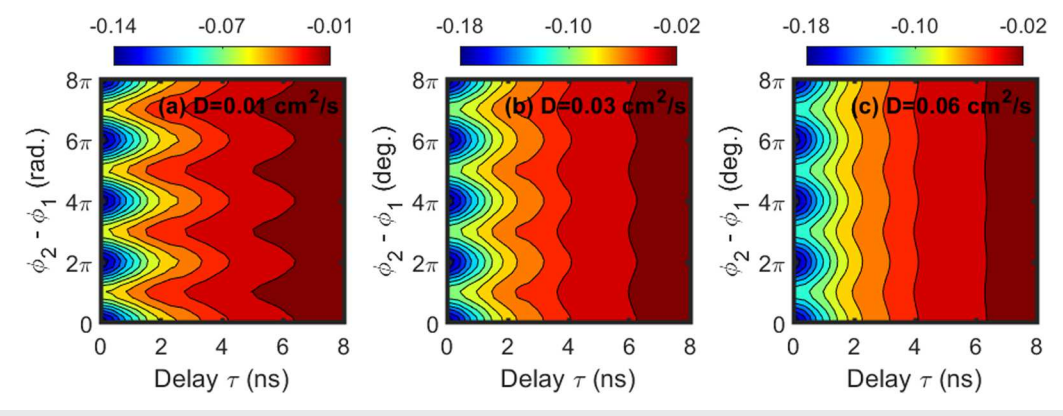


FIG. 7. TG-NLPC signals, $\Delta Q_{TG-NLPC}$, are computed as functions of the delay times and phase differences between transient density gratings, $\phi_2 - \phi_1$. Calculations are conducted using Eq. (32), the parameters in Table I, and the diffusion coefficients given in the respective panels. The color bars have units of pC.

method to carrier transport in the *y*-dimension. The periodic component of the signal decreases with the experimentally controlled delay time, τ , as diffusion takes hold in the active layer of the device. The calculation presented in Fig. 7(a) demonstrates that the experiment is relatively insensitive to diffusion when t_{diff} (~30 ns) is much greater than the transit time of carriers across the illuminated region

of the active layer (~10 ns). In contrast, relaxation of the periodic component of the signal is evident in Fig. 7(c) because the 5-ns diffusion time is less than the 10-ns timescale of carrier drift (i.e., the periodic signal component decays before the carriers are extracted from the active layer by the electrodes). Under these conditions, the diffusion coefficient of the material can be determined with an

experimental measurement by fitting the data to obtain t_{diff} and applying the relation established in Fig. 5.

IV. EXPERIMENTAL RESULTS AND DISCUSSION

In this section, we present TG-NLPC signals acquired with multiple active layer thicknesses and density grating periods. Control experiments conducted using devices with thin active layers are first presented to confirm the predicted periodic saturation effect under conditions in which drift outcompetes diffusion. Experiments conducted on devices with thicker active layers and smaller electrical potentials reveal the diffusive processes targeted by the TG-NLPC approach. Overall, the measurements presented in this section demonstrate that sufficient reduction of the drift velocity and/or grating period enable the detection of carrier diffusion.

A. Measurements conducted under conditions in which drift outcompetes diffusion

To begin, we outline our approach for processing TG-NLPC signals, which depends on both the delay times and phase differences between pulse-pairs. As shown in Fig. 8, the periodic signal component reflects the relative phases of the carrier density gratings photoexcited by separate pulse-pairs, although a portion of the response persists when the density gratings possess phase differences of π , 3π , 5π , etc. The TG-NLPC signals are fit with the following function at time-zero:

$$F(\tau,\Phi) = B_1(\tau) \cdot \sin(B_2 \cdot \Phi + B_3) + B_4(\tau) \cdot \Phi + B_5(\tau), \quad (34)$$

where τ and Φ are the experimentally controlled delay time and coverslip angle, respectively. The frequency (B_2) and phase (B_3) of the sine function are fixed after fitting the signal at the first delay point because these parameters are independent of the time interval between pulse-pairs. In contrast, the amplitude, $B_1(\tau)$, and parameters associated with the linear baseline, $B_4(\tau)$ and $B_5(\tau)$, vary with the delay time because of dynamics in the carrier densities.

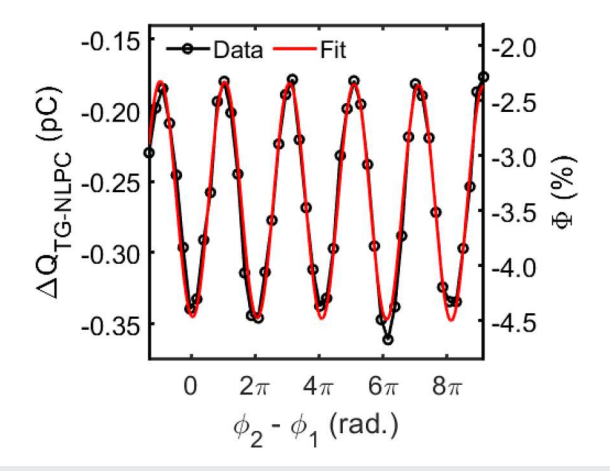


FIG. 8. TG-NLPC signals are fit using Eq. (34) with a laser fluence of 1.0 μ J/cm² per pulse and grating period of 2.15 μ m. The device has a 280-nm thick MAPbl₃ active layer, a C₆₀/BCP electron transport layer, and a PTAA hole transport layer.

The phase difference between the density gratings associated with separate pulse-pairs is given by

$$\phi_2 - \phi_1 = \Phi + \frac{\pi}{2B_2},\tag{35}$$

where the amount of saturation is maximized when $\phi_2 - \phi_1 = 0$, 2π , 4π , etc. Within the experimentally sampled range of phases (i.e., approximately five cycles), the overall rise of the baseline is much smaller than the intercept, $B_4(\tau) \cdot 10\pi \ll B_5(\tau)$. For example, we present a fit of a signal acquired with a laser fluence of $1.0~\mu\text{J/cm}^2$ and grating period of $2.15~\mu\text{m}$ in Fig. 8. The amplitude of the periodic signal component is roughly 40% of the total signal magnitude for this device. Five cycles of the grating are sampled with nine to ten points per cycle to constrain the fitting parameters.

The overall TG-NLPC signals presented in Figs. 9(a) and 9(d) must be decomposed into periodic and linear signal components to extract information from the measurements. In Figs. 9(b) and 9(e), the periodic contributions to the TG-NLPC signals are isolated by subtracting linear baselines from the data using

$$\sigma_p(\tau,\Phi) = \frac{\Delta Q_{NLPC}(\tau,\Phi) - B_4(\tau) \cdot \Phi - B_5(\tau)}{Q_1 + Q_2},$$
 (36)

where the right side of the equation is divided by $Q_1 + Q_2$ to obtain the fraction of saturation in the output of the device. For grating periods of 1.07 and 2.15 μ m, these contour plots demonstrate that the signal magnitudes decrease significantly within 5 ns for this device. The periodic,

$$\Delta Q_p(\tau) = 2B_1(\tau),\tag{37}$$

and averaged linear,

$$\Delta Q_l(\tau) = \frac{1}{M} \sum_{j=1}^{M} \left[B_4(\tau) \cdot \Phi_j + B_5(\tau) \right], \tag{38}$$

components of the fits are overlaid in Figs. 9(c) and 9(f) to show that similar decay profiles are obtained with both 1.07- and 2.15- μ m grating periods under these experimental conditions. In Eq. (38), we note that M is the number of points sampled in the coverslip angle [see Fig. 2(a)]. The data suggest that contributions of diffusion to the measurements are negligible because the periodic and linear signal components relax on essentially the same timescale for both grating periods. The calculations presented in Fig. 7(a) represent the corresponding regime in which drift outcompetes diffusion.

To understand the similar decay profiles exhibited by $\Delta Q_p(\tau)$ and $\Delta Q_l(\tau)$, the timescale of carrier diffusion can be predicted for both grating periods using the model presented in Eqs. (17)–(24) and Fig. 5. Literature values for the diffusivity of MAPbI₃ vary widely (0.02–1.77 cm²/s) depending on the fabrication conditions and measurement techniques; $^{3,10,24,25,27,70-72}$ however, transient absorption microscopy measurements conducted with similar films in our laboratory yielded diffusion coefficients with a maximum value of $D=0.033~{\rm cm}^2/{\rm s}$. If we assume a diffusion parameter of $D=0.033~{\rm cm}^2/{\rm s}$, then the calculated timescales of diffusion will be equal to ~9 and 37 ns for a 1.07- and 2.15- μ m grating periods, respectively. Thus, the carrier transit time across the 34-nm penetration depth of the incident 400-nm light must be at least 9 ns to make the TG-NLPC measurements sensitive to diffusion. However, for the

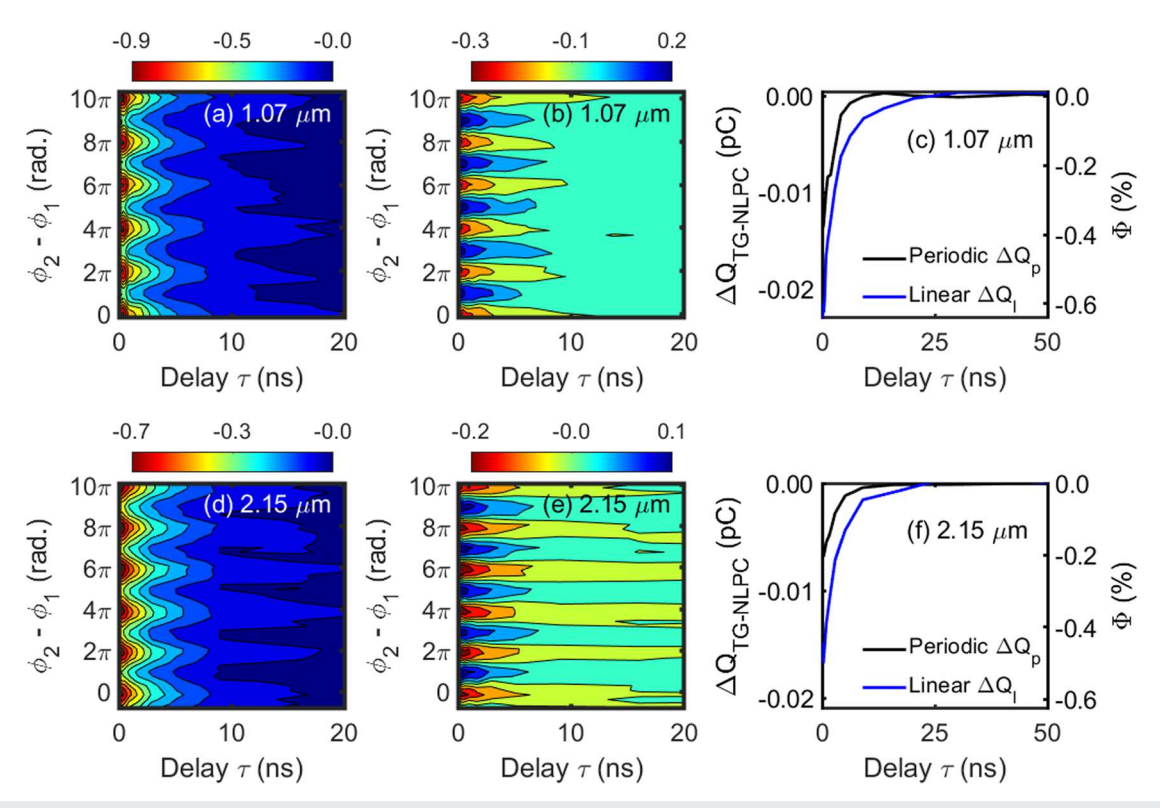


FIG. 9. TG-NLPC signals are acquired with grating periods of (a)–(c) 1.07 and (d)–(f) 2.15 μm. (a) and (d) The total signal magnitudes relax due to drift and recombination processes. (b) and (e) The periodic component of the response is separated from the total signal using Eq. (36). (c) and (f) Both periodic and linear components of the fitted signals decay within 10's of ns [see Eqs. (37) and (38)]. The device has a 280-nm thick MAPbl₃ active layer, a C₆₀/BCP electron transport layer, and a PTAA hole transport layer.

four datasets obtained using devices with 280-nm thick active layers (see the supplementary material), the periodic and linear components of the signals decay to 1/e of their initial values within 5 ns, which explains the insensitivity of the results shown in Fig. 9 to the grating period. Nonetheless, because this is the first application of a new technique, these measurements constitute an important control for confirming that the targeted signatures of diffusivity are absent when drift outcompetes diffusion.

B. Probing carrier diffusion by reducing drift velocities

The measurements presented in Sec. IV A were conducted with a device possessing a 280-nm active layer thickness and relatively optimal electron (C_{60} /BCP) and hole (PTAA) transport layers. These experiments serve as important controls for confirming the predicted signal generation mechanism under conditions in which drift dominates the temporal decay of the periodic signal component. In contrast, the model calculations discussed in Sec. III show that diffusive processes can be probed with TG-NLPC measurements if the carrier transit time is greater than the diffusion time, t_{diff} . According to Eq. (33), the transit time can be experimentally controlled by applying an external potential to the device; however, we find that the efficiencies of the photovoltaic cells can degrade when external

potentials are applied over data acquisition times of 4–10 h. Therefore, we conduct experiments on devices with modified thicknesses and transport layers in this section to observe diffusion without applying external potentials. We reiterate that degradations in the responses of the devices are not observed during data acquisition when external biases are not applied. The device efficiencies and TG-NLPC signal line shapes are maintained over the full data acquisition times (see the supplementary material).

To extract diffusivities from TG-NLPC experiments, we employ a photovoltaic device with a 480-nm active layer thickness to reduce the electric field within the active layer. Notably, the electric field scales as the inverse of the MAPbI₃ active layer thickness under the assumption that the potential varies linearly with position. In addition, PEDOT:PSS and C₆₀/BCP are employed as the hole and electron transport layers, respectively. This combination of transport layers produces an open-circuit voltage of ~0.7 V, whereas the devices fabricated with PTAA have open-circuit voltages of ~1.0 V. Although the comparison is approximate, we remark that the opencircuit voltage of the device with the PEDOT:PSS hole transport layer is in good agreement with the predicted 0.68-V threshold for detection of diffusion predicted by Eq. (33). Furthermore, an energy level mismatch between MAPbI₃ and PEDOT:PSS may decrease the rate at which holes cross the interface between materials.⁷³ Most importantly, these fabrication conditions increase the empirical

TG-NLPC decay times by close to a factor of 10, which is sufficient for measurements of diffusion in MAPbI₃ according to the estimation discussed in Sec. IV A.

The signals presented in Fig. 10 are processed using the same approach applied to the data in Fig. 9. The plots employ logarithmic delay axes because the signals fully decay over 100's of ns due to the inflated carrier transit times. The total signals displayed in Figs. 10(a) and 10(d) exhibit similar features; however, differences in the timescales of the relaxation processes are apparent for the isolated periodic signal components, $\sigma_p(\tau, \Phi)$, shown in Figs. 10(b) and 10(e). In Fig. 10 and our additional datasets (see the supplementary material), we find that the transient density grating persists for a greater length of time when the period increases from 1.07 to 2.15 μ m. For example, in Figs. 10(b) and 10(e), the darker blue and orange contours in the periodic patterns vanish in less than 10 ns with a 1.07- μ m period, whereas these features persist for more than 10 ns when the period is equal to 2.15 μ m. Finally, the periodic and linear signal components of the fits, $\Delta Q_p(\tau)$ and $\Delta Q_l(\tau)$, are displayed in Figs. 10(c) and 10(f). The shapes of these decay profiles encode the targeted signatures of carrier diffusion.

Periodic and linear components of TG-NLPC signals are summarized for four pairs of experiments in Fig. 11. The linear components of the signals, $\Delta Q_l(\tau)$, are fit using a sum of exponential functions,

$$S_l(\tau) = C_1 \exp(-\tau/T_1) + C_2 \exp(-\tau/T_2),$$
 (39)

where the weighted averages of time constants reported in Table II are given by

$$T_{av} = \frac{C_1 T_1}{C_1 + C_1} + \frac{C_2 T_2}{C_1 + C_1}. (40)$$

These fits reveal that the decay in the linear component of carrier density occurs in $T_{av}=32$ and 51 ns for experiments performed with grating periods of 1.07 and 2.15 μ m, respectively. Shorter decay times are measured with the 1.07- μ m period due to the dynamic redistribution of the periodic and Gaussian components of the density grating in the active layer [see Eq. (17)]. Diffusion diminishes the periodic part of the carrier density; however, the number of

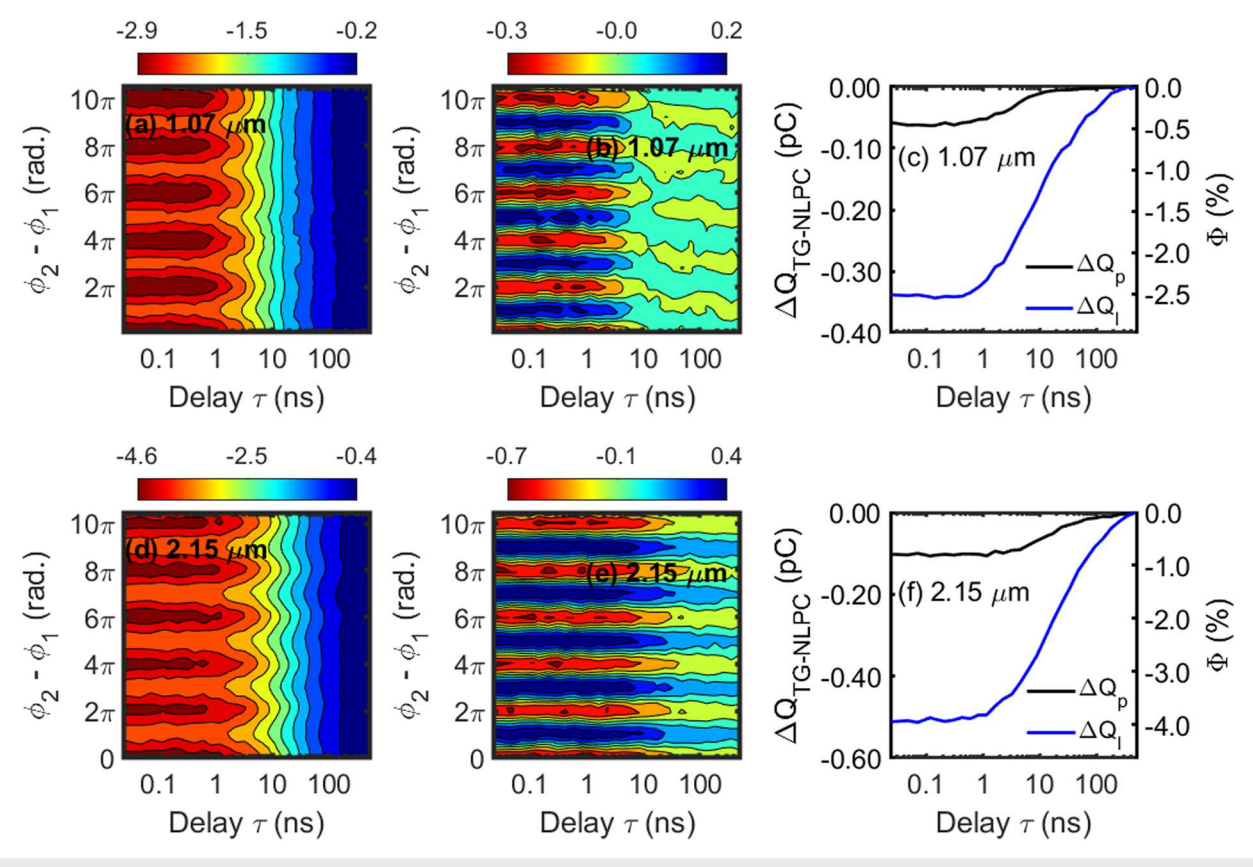


FIG. 10. TG-NLPC signals are acquired with grating periods of (a)–(c) 1.07 and (d)–(f) 2.15 μm. (a) and (d) The total signal magnitudes relax due to drift and recombination processes. (b) and (e) The periodic component of the response is separated from the total signal using Eq. (36). (c) and (f) Both periodic and linear components of the fitted signals relax within 100's of ns [see Eqs. (37) and (38)]. The device has a 480-nm thick MAPbl₃ active layer, a C₆₀/BCP electron transport layer, and a PEDOT:PSS hole transport layer.

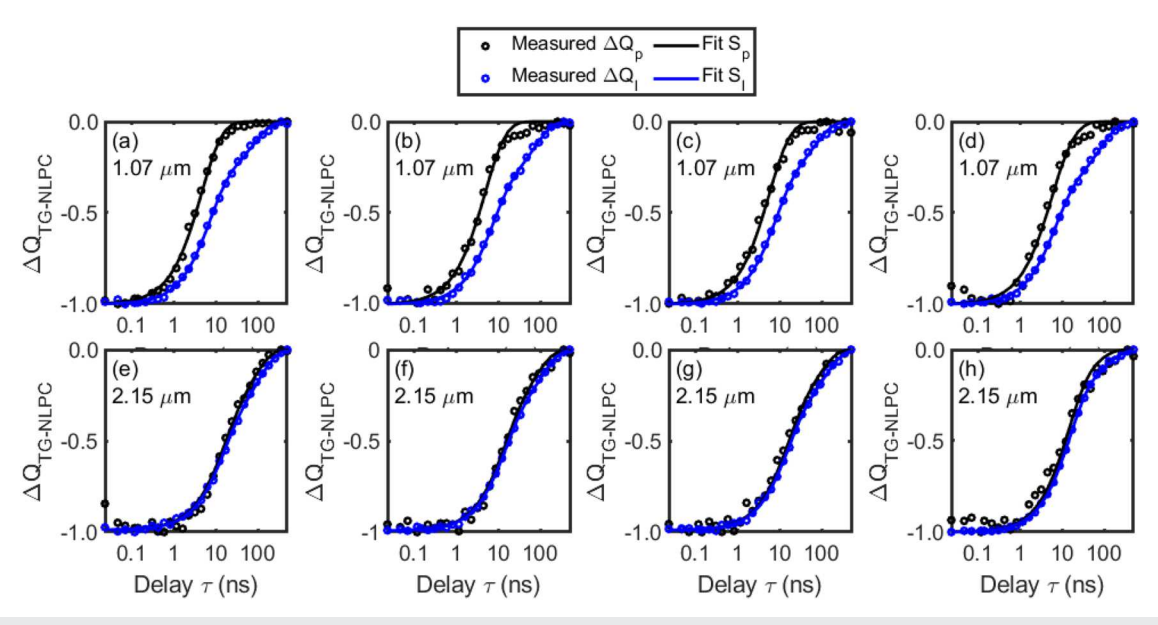


FIG. 11. Normalized periodic and linear components of TG-NLPC signals are fit with grating periods of (a)–(d) 1.07 and (e)–(h) 2.15 μ m. Diffusive processes are evident when the grating period is equal to 1.07 μ m; however, the periodic and linear signal components are indistinguishable when the grating period is 2.15 μ m due to the corresponding increase in the diffusion timescale. These devices have 480-nm thick active layers, a C₆₀/BCP electron transport layer, and a PEDOT:PSS hole transport layer.

carriers associated with the Gaussian part of the TG-NLPC response, which contributes to $\Delta Q_l(\tau)$, simultaneously increases because the diffusion process conserves the total number of carriers in the active layer; the integrated area of $G(y,t',\phi_j)$ is independent of the time variable, t', in Eq. (17). Therefore, because the recombination rate increases with the carrier density, transferring carriers from the periodic to Gaussian components of the density profile accelerates the decay of $\Delta Q_l(\tau)$.

Empirical diffusion times are obtained by multiplying $S_I(\tau)$ with an exponential envelope function,

$$S_{D}(\tau) = S_{I}(\tau) \exp\left(-\tau/t_{diff}\right),\tag{41}$$

and fitting the periodic component of the signal, $\Delta Q_p(\tau)$. The diffusion coefficient can then be determined by comparing the empirical value of t_{diff} to the model calculation presented in Fig. 5. For the 1.07- μ m grating period, an average diffusion coefficient of

TABLE II. TG-NLPC Fitting Parameters.

Parameter	$1.07~\mu\mathrm{m}$	2.15 μm			
$T_{av} \ t_{diff}^{}^{^{}}}}}}}}}}}}}}}}}}}}}}}}}}}}}}}}}}$	$32.44 \pm 2.91 \text{ ns}$ $11.06 \pm 2.44 \text{ ns}$ $0.028 \pm 0.006 \text{ cm}^2/\text{s}$	50.77 ± 8.66 ns 229.09 ± 76.87 ns			

^aThe uncertainty range for t_{diff} represents the standard deviation associated with the four results displayed in Fig. 11. This fitting parameter directly reflects relaxation of the periodic signal component and does not require solution of a diffusion equation.

 $D = 0.028 \text{ cm}^2/\text{s}$ is obtained with the four datasets presented in Fig. 11. Notably, this diffusion coefficient is within the uncertainty ranges of the diffusivities we have previously determined using transient absorption microscopies conducted on similar MAPbI₃ films.²⁷ In the bottom row of Fig. 11, the TG-NLPC experiments performed with a 2.15-µm grating period are not useful for determining diffusion coefficients; however, these measurements constitute controls for confirming that the signature of diffusivity is suppressed when the grating period increases. It is instructive to consider that the diffusion time for a density grating roughly scales as the square of the period, L, because carriers diffuse toward the concentration minima from two directions. For example, with a diffusion coefficient of $D = 0.03 \text{ cm}^2/\text{s}$, we compute diffusion times of $t_{diff} = 10$ and 39 ns for gratings periods of 1.07 and 2.15 μ m using Eqs. (17)–(24). This fourfold discrepancy in diffusion times is consistent with the behaviors observed in Fig. 11.

The diffusion coefficient determined with the TG-NLPC technique, $D=0.028~{\rm cm^2/s}$, can be put in perspective with consideration of the $\mu=0.025\text{-cm^2/V/s}$ mobility measured with NLPC spectroscopy for MAPbI₃ devices in our laboratory. Under the assumption of a sufficiently weak electric field within the active layer, the diffusion coefficient is related to the carrier mobility by the Einstein–Smoluchowski equation,

$$D = \frac{\mu \cdot k_B T}{q_e},\tag{42}$$

where q_e is the electrical charge. Thus, the diffusion coefficient predicted with the empirical mobility, $D = 0.0006 \, \mathrm{cm}^2/\mathrm{s}$, is ~44 times smaller than the measured value of $D = 0.028 \, \mathrm{cm}^2/\mathrm{s}$. Considering that diffusivities can vary by orders of magnitude depending on

^bThe uncertainty range in D is translated from t_{diff} using the relation shown in Fig. 5. Heterogeneity in the refractive index on the micrometer length scale can additionally inflate the uncertainty in the D.

the measurement technique,⁵ we attribute this discrepancy to differences in the length scales and directions of transport associated with conventional NLPC and TG-NLPC measurements.⁵ In the present TG-NLPC measurements, the diffusivity reflects lateral motions of carriers (i.e., orthogonal to the direction of drift) on the length scale of 1.07 μ m for the smallest grating period. In contrast, the mobilities obtained with conventional NLPC spectroscopy are sensitive to transport between electrodes on the length scale of the light penetration depth (e.g., 34 nm for MAPbI₃ at an incident wavelength of 400 nm). ^{32,69} For these reasons, we suggest that the carrier mobilities and diffusivities determined NLPC and TG-NLPC spectroscopies will generally carry complementary information.

C. Practical considerations for generalizing the TG-NLPC method to other materials

Model calculations and control experiments have been used to characterize TG-NLPC signal generation mechanisms in the present work. In this section, we summarize the practical implications of our results for applications to other materials.

First, we clarify that TG-NLPC experiments possess a low technical barrier compared to femtosecond nonlinear spectroscopies. As discussed in our recent work, 32 the present NLPC setup employs a pair of synchronized 40-ps, 400-nm diode lasers, whereas our initial NLPC experiments were based on an amplified titanium–sapphire laser system. $^{29-31}$ Therefore, it is not necessary to compress the laser pulses, and the delay time is varied without a mechanical translation stage. The entire path from the laser system to the sample includes a total of ten mirrors. The TG-NLPC interferometer, which is adapted from diffractive optic-based four-wave mixing approaches, $^{54-57}$ is straightforward to align and maintains passive phase stabilization for at least 24 h. Moreover, the saturation response targeted by the technique is typically 1%-5% with $1-\mu J/cm^2$ laser fluences, two-body recombination coefficients on the order of 10^{-9} cm³/s, and excited-state lifetimes exceeding $1~\mu$ s. 33

Second, we have shown that diffusion cannot be detected if carriers drift to the electrodes on a shorter timescale. For this reason, the transport layers of the devices were altered in this work to reduce the carrier drift velocities, whereas the timescale of diffusion was varied using the density grating periods. To generalize the method to arbitrary materials and devices, we suggest that the grating period can be reduced to ensure that the timescale of diffusion is always shorter than the carrier transit time between electrodes. For example, diffusion times less than 5 ns can be achieved with a grating period of 500 nm assuming the diffusion coefficient is at least $D = 0.03 \, \mathrm{cm}^2/\mathrm{s}$. The method will then be compatible with perovskite photovoltaic devices possessing active layer thicknesses of ~100 nm (i.e., carrier transit times exceeding 10 ns). $^{29-31}$

Third, whereas the linear optical properties of MAPbI₃ films have been fully characterized,⁶⁹ the refractive indices must be measured for all newly developed materials (e.g., with ellipsometry) to compute the periods of density gratings using Eq. (19). Like conventional transient grating spectroscopies, the refractive index of the sample must be known to determine diffusion coefficients with the TG-NLPC method. In contrast, the diffusion timescales are found by fitting the TG-NLPC signals and do not require modeling the signal generation mechanism (see Fig. 11).

Fourth, because the time resolution of the technique reflects a sub-ns "burst" of carrier recombination,³³ it is not necessary to numerically deconvolute recombination dynamics from slower drift and diffusion processes. For example, the model presented in Sec. III suggests that relaxation of the periodic signal component (see Fig. 8) directly reflects diffusion if recombination processes accumulate on a shorter timescale. The same principle applies to carrier drift and has been verified with time-of-flight measurements conducted under a variety of conditions.^{29,30,32,74} While NLPC spectroscopies are compatible with studies of nanosecond transport mechanisms, they have limited use for studies of picosecond electron and energy transfer mechanisms.³³ Multidimensional photocurrent spectroscopies based on higher-order perturbative responses are capable of femtosecond time resolution but are more challenging to implement.^{34–37,75–77}

V. CONCLUDING REMARKS

In recent years, we have developed multi-pulse photocurrent spectroscopies in which recombination-induced nonlinearities are leveraged for studies of long-range transport mechanisms in perovskite photovoltaic cells. ^{28–33} These methods take inspiration from traditional four-wave mixing techniques $^{78-80}$ and Fourier transform multidimensional photocurrent action spectroscopies,³⁴ where a nonlinear polarization is induced within a material using a sequence of laser pulses. Such nonlinear polarizations, which are described using higher-order time-dependent perturbation theory,81 encode information regarding transient populations and resonances between excited states. The recombination-induced nonlinearities targeted in the present work can be viewed as a nuisance in Fourier transform photocurrent spectroscopies because of differences in time resolution and information content. 36,38,41,82 Nonetheless, we have demonstrated that NLPC signals yield dynamical information unlike the cascades of lower-order responses observed in two-dimensional off-resonant Raman spectroscopies.8

Although recombination-induced nonlinearities cannot reveal resonances between excited states or femtosecond dynamics, the signals mimic spectroscopic signatures observed in conventional multidimensional optical spectroscopies on longer timescales. For example, two-dimensional NLPC spectra acquired with a pair of colortunable laser pulses exhibit dynamic growth in cross-peaks due to charge carrier funneling in mixtures of layered perovskite quantum wells.³⁰ In addition, energy funneling processes yield similar spectroscopic features in recombination-induced two-dimensional fluorescence spectra acquired for layered perovskite systems because of related signal generation mechanisms. 28,33 Whereas the magnitudes of cross-peaks represent transient occupations of specific quantum wells in NLPC experiments, saturation of the photocurrent induced by carrier recombination processes partly flattens the spectroscopic line shapes. In addition, the time resolution of the NLPC method is limited by rate at which recombination processes accumulate in the active layer. 31-33 For example, the time resolution for NLPC spectroscopy is near 100 ps for experiments conducted with 1-µJ/cm² laser fluences and materials with recombination coefficients of $\beta = 10^{-9} \text{ cm}^2/\text{s.}^{32,33}$ Therefore, NLPC experiments are best-suited to studies of long-range transport on nanosecond timescales.

Like two-dimensional NLPC experiments,³⁰ the TG-NLPC technique introduced in this work combines nonlinear optical and

time-of-flight concepts to establish a comprehensive understanding of the dynamics occurring within the active layer of a device. Although drift and diffusion are subject to a fluctuation-dissipation relation, 19 complementary information regarding the two transport mechanisms is obtained with the TG-NLPC method because the dynamics are probed in orthogonal directions. The direction of carrier transport is significant because the grains sizes and crystalline structural orientations can vary within the active layers of MAPbI₃ devices depending on the fabrication conditions.⁴ Moreover, the present experiments are sensitive to drift on the length scale of the light penetration depth (34 nm in MAPbI₃ with an incident wavelength of 400 nm), ^{32,69} whereas diffusion is probed using density gratings with periods of at least 1.07 µm. Although we have focused on the dynamics of free charge carriers in this work, the TG-NLPC approach can be supplemented with a fluorescence detection channel to probe exciton diffusion in systems such as layered perovskite quantum wells, where excitons constitute more than 90% of the photoexcited species and dominate spontaneous emission.^{28,5} Experiments conducted with dual photocurrent and fluorescence detection channels^{28,33} can enable a rapid characterization of transport mechanisms for both free charge carriers (drift and diffusion) and excitons (diffusion) in heterogeneous materials.

SUPPLEMENTARY MATERIAL

We present background related to the transient grating beam geometry, calculations associated with the model for diffusion, TG-NLPC data acquired for additional devices, SEM images displaying the active layer thicknesses, and data demonstrating the stabilities of the devices during data acquisition.

ACKNOWLEDGMENTS

This work was supported by the National Science Foundation under Grant Nos. CHE-1763207 (Z.O., Z.G., and A.M.M.) and CHE-2154791 (L.Y. and W.Y.). This work was performed in part at the Chapel Hill Analytical and Nanofabrication Laboratory, CHANL, a member of the North Carolina Research Triangle Nanotechnology Network, RTNN, which is supported by the National Science Foundation, Grant No. ECCS-2025064, as part of the National Nanotechnology Coordinated Infrastructure, NNCI.

AUTHOR DECLARATIONS

Conflict of Interest

The authors have no conflicts to disclose.

Author Contributions

Z.O. and Z.G. contributed equally to this work.

Zhenyu Ouyang: Data curation (equal); Project administration (supporting); Writing – original draft (supporting). Zijian Gan: Data curation (equal); Project administration (supporting); Writing – original draft (supporting). Liang Yan: Investigation (supporting); Resources (supporting); Writing – original draft

(supporting). **Wei You**: Funding acquisition (supporting); Project administration (supporting); Resources (equal); Writing – original draft (supporting). **Andrew M. Moran**: Conceptualization (equal); Funding acquisition (equal); Project administration (equal); Resources (equal); Writing – original draft (equal).

DATA AVAILABILITY

The data that support the findings of this study are available from the corresponding author upon reasonable request.

REFERENCES

- ¹D. Shi, V. Adinolfi, R. Comin, M. Yuan, E. Alarousu, A. Buin, Y. Chen, S. Hoogland, A. Rothenberger, K. Katsiev, Y. Losovyj, X. Zhang, P. A. Dowben, O. F. Mohammed, E. H. Sargent, and O. M. Bakr, Science 347(6221), 519 (2015).
- ²Q. Dong, Y. Fang, Y. Shao, P. Mulligan, J. Qiu, L. Cao, and J. Huang, Science 347(6225), 967 (2015).
- ³ Z. Guo, J. S. Manser, Y. Wan, P. V. Kamat, and L. Huang, Nat. Commun. **6**(1), 7471 (2015).
- ⁴B. Zhang, M.-J. Zhang, S.-P. Pang, C.-S. Huang, Z.-M. Zhou, D. Wang, N. Wang, and G.-L. Cui, Adv. Mater. Interfaces 3(17), 1600327 (2016).
- ⁵L. M. Herz, Annu. Rev. Phys. Chem. **67**(1), 65–89 (2016).
- ⁶ A. H. Hill, C. L. Kennedy, E. S. Massaro, and E. M. Grumstrup, J. Phys. Chem. Lett. 9(11), 2808–2813 (2018).
- ⁷W. Shcherbakov-Wu and W. A. Tisdale, Chem. Sci. 11(20), 5157–5167 (2020).
- ⁸M. Seitz, A. J. Magdaleno, N. Alcázar-Cano, M. Meléndez, T. J. Lubbers, S. W. Walraven, S. Pakdel, E. Prada, R. Delgado-Buscalioni, and F. Prins, Nat. Commun. 11(1), 2035 (2020).
- ⁹X. Xiao, M. Wu, Z. Ni, S. Xu, S. Chen, J. Hu, P. N. Rudd, W. You, and J. Huang, Adv. Mater. **32**(46), 2004080 (2020).
- ¹⁰S. Deng, E. Shi, L. Yuan, L. Jin, L. Dou, and L. Huang, Nat. Commun. 11(1), 664 (2020).
- ¹¹ M. Sajedi Alvar, P. W. M. Blom, and G.-J. A. H. Wetzelaer, Nat. Commun. 11, 4023 (2020).
- ¹²C. L. Hickey and E. M. Grumstrup, Nano Lett. **20**(7), 5050–5056 (2020).
- ¹³ A. Bou, H. Abolinš, A. Ashoka, H. Cruanyes, A. Guerrero, F. Deschler, and J. Bisquert, ACS Energy Lett. 6(6), 2248–2255 (2021).
- ¹⁴S. Shrestha, X. Li, H. Tsai, C.-H. Hou, H.-H. Huang, D. Ghosh, J.-J. Shyue, L. Wang, S. Tretiak, X. Ma, and W. Nie, Chem 8(4), 1107–1120 (2022).
- ¹⁵N. Nagaya Wong, S. K. Ha, K. Williams, W. Shcherbakov-Wu, J. W. Swan, and W. A. Tisdale, J. Chem. Phys. 157(10), 104201 (2022).
- ¹⁶D. Seyitliyev, X. Qin, M. K. Jana, S. M. Janke, X. Zhong, W. You, D. B. Mitzi, V. Blum, and K. Gundogdu, Adv. Funct. Mater. 33, 2213021 (2023).
- ¹⁷X. Jiang, S. Jun, J. Hoffman, M. G. Kanatzidis, and E. Harel, J. Phys. Chem. A 124(23), 4837–4847 (2020).
- ¹⁸S. Chandrasekhar, Rev. Mod. Phys. **15**(1), 1–89 (1943).
- ¹⁹R. Kubo, Rep. Prog. Phys. **29**(1), 255–284 (1966).
- ²⁰ L. M. Schwartz and J. F. Hornig, J. Phys. Chem. Solids 26(12), 1821–1824 (1965).
- ²¹ W. E. Spear, J. Non-Cryst. Solids 1(3), 197–214 (1969).
- ²²T. Bronger, in *Advanced Characterization Techniques for Thin Film Solar Cells*, edited by D. Abou-Ras, T. Kirchartz, and U. Rau (Wiley VCH, Weinheim, 1991), Vol. 1, pp. 121–145.
- ²³ N. Karl, in *Organic Electronic Materials Conjugated Polymers and Low Molecular Weight Organic Solids*, edited by R. Farchoni and G. Grosso (Springer-Verlag, New York, 2001).
- ²⁴G. Xing, N. Mathews, S. Sun, S. S. Lim, Y. M. Lam, M. Grätzel, S. Mhaisalkar, and T. C. Sum, Science 342, 344–347 (2013).
- ²⁵S. D. Stranks, G. E. Eperon, G. Grancini, C. Menelaou, M. J. P. Alcocer, T. Leijtens, L. M. Herz, A. Petrozza, and H. J. Snaith, Science **342**(6156), 341–344 (2013).
- ²⁶S. Nah, B. Spokoyny, C. Stoumpos, C. M. M. Soe, M. Kanatzidis, and E. Harel, Nat. Photonics 11(5), 285–288 (2017).

- ²⁷Z. Guo, N. Zhou, O. F. Williams, J. Hu, W. You, and A. M. Moran, J. Phys. Chem. C 122(19), 10650–10656 (2018).
- ²⁸ N. Zhou, Z. Ouyang, J. Hu, O. F. Williams, L. Yan, W. You, and A. M. Moran, J. Phys. Chem. Lett. 11(12), 4570–4577 (2020).
- ²⁹ N. Zhou, Z. Ouyang, L. Yan, M. G. McNamee, W. You, and A. M. Moran, J. Phys. Chem. Lett. **12**(4), 1116–1123 (2021).
- ³⁰Z. Ouyang, N. Zhou, M. G. McNamee, L. Yan, O. F. Williams, W. You, and A. M. Moran, J. Chem. Phys. **154**(22), 220901 (2021).
- ³¹ Z. Ouyang, N. Zhou, M. G. McNamee, L. Yan, O. F. Williams, Z. Gan, R. Gao, W. You, and A. M. Moran, J. Chem. Phys. **156**(8), 084202 (2021).
- ³²Z. Ouyang, L. Yan, W. You, and A. M. Moran, J. Chem. Phys. 157(17), 174202 (2022).
- ³³ M. G. McNamee, Z. Ouyang, L. Yan, Z. Gan, N. Zhou, O. F. Williams, W. You, and A. M. Moran, J. Phys. Chem. C **127**(6), 2782–2791 (2023).
- ³⁴G. Nardin, T. M. Autry, K. L. Silverman, and S. T. Cundiff, Opt. Express 21(23), 28617–28627 (2013).
- ³⁵ K. J. Karki, J. R. Widom, J. Seibt, I. Moody, M. C. Lonergan, T. Pullerits, and A. H. Marcus, Nat. Commun. 5(1), 5869 (2014).
- ³⁶P. Grégoire, A. R. Srimath Kandada, E. Vella, C. Tao, R. Leonelli, and C. Silva, J. Chem. Phys. **147**(11), 114201 (2017).
- ³⁷F. A. Damtie, A. Wacker, T. Pullerits, and K. J. Karki, Phys. Rev. A **96**(5), 053830 (2017)
- ³⁸ A. A. S. Kalaee, F. Damtie, and K. J. Karki, J. Phys. Chem. A **123**(19), 4119–4124 (2019).
- ³⁹ K. Wang, R. A. Muniz, J. E. Sipe, and S. T. Cundiff, Phys. Rev. Lett. **123**(6), 067402 (2019).
- ⁴⁰L. Bolzonello, F. Bernal-Texca, L. G. Gerling, J. Ockova, E. Collini, J. Martorell, and N. F. van Hulst, J. Phys. Chem. Lett. 12(16), 3983–3988 (2021).
- ⁴¹I. Bargigia, E. Gutiérrez-Meza, D. A. Valverde-Chávez, S. R. Marques, A. R. Srimath Kandada, and C. Silva, J. Chem. Phys. 157(20), 204202 (2022).
- Strimath Randada, and C. Silva, J. Chem. Phys. 157(20), 204202 (2022).

 42 Q. Lin, A. Armin, R. C. R. Nagiri, P. L. Burn, and P. Meredith, Nat. Photonics
- **9**(2), 106–112 (2015). ⁴³ B. Maynard, Q. Long, E. A. Schiff, M. Yang, K. Zhu, R. Kottokkaran, H. Abbas,
- and V. L. Dalal, Appl. Phys. Lett. **108**(17), 173505 (2016).

 44F. Ebadi, N. Taghavinia, R. Mohammadpour, A. Hagfeldt, and W. Tress, Nat.
- Commun. 10(1), 1574 (2019).
- ⁴⁵G. S. Schlau-Cohen, A. Ishizaki, and G. R. Fleming, Chem. Phys. **386**(1–3), 1–22 (2011).
- ⁴⁶Y. Lee, M. Gorka, J. H. Golbeck, and J. M. Anna, J. Am. Chem. Soc. **140**(37), 11631–11638 (2018).
- ⁴⁷S. Irgen-Gioro, K. Gururangan, R. G. Saer, R. E. Blankenship, and E. Harel, Chem. Sci. **10**(45), 10503–10509 (2019).
- ⁴⁸S. Higgins Jacob, A. Allodi Marco, T. Lloyd Lawson, P. Otto John, H. Sohail Sara, G. Saer Rafael, E. Wood Ryan, C. Massey Sara, P.-C. Ting, E. Blankenship Robert, and S. Engel Gregory, Proc. Natl. Acad. Sci. U. S. A. 118(49), e2112817118 (2021).
- ⁴⁹Y. Song, R. Sechrist, H. H. Nguyen, W. Johnson, D. Abramavicius, K. E. Redding, and J. P. Ogilvie, Nat. Commun. 12(1), 2801 (2021).
- ⁵⁰S. Biswas, J. Kim, X. Zhang, and G. D. Scholes, Chem. Rev. **122**(3), 4257–4321 (2022).
- ⁵¹ S. Sil, R. W. Tilluck, N. Mohan T, C. H. Leslie, J. B. Rose, M. A. Domínguez-Martín, W. Lou, C. A. Kerfeld, and W. F. Beck, Nat. Chem. 14(11), 1286–1294 (2022).
- ⁵²E. Collini, J. Phys. Chem. C **125**(24), 13096–13108 (2021).
- ⁵³ R. Trebino, K. W. DeLong, D. N. Fittinghoff, J. N. Sweetser, M. A. Krumbügel, B. A. Richman, and D. J. Kane, Rev. Sci. Instrum. 68(9), 3277–3295 (1997).
- ⁵⁴G. D. Goodno, G. Dadusc, and R. J. D. Miller, J. Opt. Soc. Am. B 15(6), 1791–1794 (1998).
- ⁵⁵ A. A. Maznev, K. A. Nelson, and J. A. Rogers, Opt. Lett. 23(16), 1319-1321 (1998).

- ⁵⁶Q.-H. Xu, Y.-Z. Ma, and G. R. Fleming, Chem. Phys. Lett. **338**(4–6), 254–262 (2001).
- ⁵⁷ A. M. Moran, J. B. Maddox, J. W. Hong, J. Kim, R. A. Nome, G. C. Bazan, S. Mukamel, and N. F. Scherer, J. Chem. Phys. **124**(19), 194904 (2006).
- ⁵⁸G. D. Goodno, V. Astinov, and R. J. D. Miller, J. Phys. Chem. B **103**(4), 603–607 (1999).
- ⁵⁹N. Gedik and J. Orenstein, Opt. Lett. **29**(18), 2109–2111 (2004).
- ⁶⁰S. Park, J. Kim, A. M. Moran, and N. F. Scherer, Phys. Chem. Chem. Phys. **13**(1), 214–223 (2011).
- ⁶¹B. A. West and A. M. Moran, J. Phys. Chem. Lett. 3(18), 2575–2581 (2012).
- ⁶² B. P. Molesky, P. G. Giokas, Z. Guo, and A. M. Moran, J. Chem. Phys. **141**(11), 114202 (2014).
- ⁶³T. Tiedje and A. Rose, Solid State Commun. **37**(1), 49–52 (1981).
- ⁶⁴T. Tiedje, in *The Physics of Hydrogenated Amorphous Silicon II: Electronic and Vibrational Properties*, edited by Joannopoulos and G. Lucovsky (Springer, Berlin, 1984), Vol. 56, pp. 261–300.
- ⁶⁵O. F. Williams, Z. Guo, J. Hu, L. Yan, W. You, and A. M. Moran, J. Chem. Phys. 148(13), 134706 (2018).
- ⁶⁶O. F. Williams, N. Zhou, J. Hu, Z. Ouyang, A. Kumbhar, W. You, and A. M. Moran, J. Phys. Chem. A **123**(51), 11012–11021 (2019).
- 67 W. Shockley and W. T. Read, Phys. Rev. 87(5), 835-842 (1952).
- ⁶⁸P. T. Landsberg, Recombination in Semiconductors (Cambridge University Press, Cambridge, 1991).
- ⁶⁹P. Löper, M. Stuckelberger, B. Niesen, J. Werner, M. Filipič, S.-J. Moon, J.-H. Yum, M. Topič, S. De Wolf, and C. Ballif, J. Phys. Chem. Lett. 6(1), 66–71 (2015).
- ⁷⁰T. J. Savenije, C. S. Ponseca, L. Kunneman, M. Abdellah, K. Zheng, Y. Tian, Q. Zhu, S. E. Canton, I. G. Scheblykin, T. Pullerits, A. Yartsev, and V. Sundström, J. Phys. Chem. Lett. 5(13), 2189–2194 (2014).
- ⁷¹ W. Tian, C. Zhao, J. Leng, R. Cui, and S. Jin, J. Am. Chem. Soc. 137(39), 12458–12461 (2015).
- ⁷² A. H. Hill, K. E. Smyser, C. L. Kennedy, E. S. Massaro, and E. M. Grumstrup, J. Phys. Chem. Lett. 8(5), 948–953 (2017).
- ⁷³ W. Han, G. Ren, J. Liu, Z. Li, H. Bao, C. Liu, and W. Guo, ACS Appl. Mater. Interfaces 12(44), 49297–49322 (2020).
- ⁷⁴N. Zhou, Z. Ouyang, M. McNamee, O. F. Williams, Z. Guo, L. Yan, J. Hu, W. You, and A. M. Moran, J. Phys. Chem. C **125**(15), 8021–8030 (2021).
- ⁷⁵E. Vella, H. Li, P. Grégoire, S. M. Tuladhar, M. S. Vezie, S. Few, C. M. Bazán, J. Nelson, C. Silva-Acuña, and E. R. Bittner, Sci. Rep. 6(1), 29437 (2016).
- ⁷⁶A. A. Bakulin, C. Silva, and E. Vella, J. Phys. Chem. Lett. 7(2), 250–258 (2016).
- 77 M. Bruschi, L. Bolzonello, F. Gallina, and B. Fresch, J. Phys. Chem. Lett. 14(30), 6872–6879 (2023).
- ⁷⁸D. M. Jonas, Annu. Rev. Phys. Chem. **54**(1), 425–463 (2003).
- ⁷⁹ T. Brixner, T. Mančal, I. V. Stiopkin, and G. R. Fleming, J. Chem. Phys. **121**(9), 4221–4236 (2004).
- ⁸⁰J. P. Ogilvie and K. J. Kubarych, *Advances in Atomic, Molecular, and Optical Physics* (Academic Press, 2009), Vol. 57, pp. 249–321.
- ⁸¹S. Mukamel, Principles of Nonlinear Optical Spectroscopy (Oxford University Press, New York, 1995).
- ⁸²O. Kühn, T. Mančal, and T. Pullerits, J. Phys. Chem. Lett. 11(3), 838–842 (2020).
- ⁸³ D. J. Ulness, J. C. Kirkwood, and A. C. Albrecht, J. Chem. Phys. **108**(10), 3897–3902 (1998).
- 84 D. A. Blank, L. J. Kaufman, and G. R. Fleming, J. Chem. Phys. 111(7), 3105–3114 (1999)
- ⁸⁵ K. J. Kubarych, C. J. Milne, S. Lin, V. Astinov, and R. J. D. Miller, J. Chem. Phys. 116(5), 2016–2042 (2002).
- ⁸⁶R. D. Mehlenbacher, B. Lyons, K. C. Wilson, Y. Du, and D. W. McCamant, J. Chem. Phys. **131**(24), 244512 (2009).